Review

High-Mobility Topological Semimetals as Novel Materials for Huge Magnetoresistance Effect and New Type of Quantum Hall Effect

Roberto Zivieri *, Stefano Lumetti, Jérémy Létang

Posted Date: 13 November 2023

doi: 10.20944/preprints202311.0757.v1

Keywords: Topological semimetals, Band structure, Magnetotransport properties, Carrier mobility, Magnetoresistance sensors; Magnetoresistance effect; 3D quantum Hall effect

Article

High-Mobility Topological Semimetals as Novel Materials for Huge Magnetoresistance Effect and New Type of Quantum Hall Effect

Roberto Zivieri [1,*], Stefano Lumetti [2] and Jérémy Létang [2]

[1] Consorzio Futuro in Ricerca (CFR), Ferrara, Italy
[2] Silicon Austria Labs, Villach, Austria
* Correspondence: roberto.zivieri@unife.it

Abstract: During the last decades the quantitative description of electrical and magnetotransport properties of solid-state materials has been a remarkable challenge in materials science. Recently, the discovery of a novel class of materials, the topological semimetals, has led to a growing interest for the full understanding of their magnetotransport properties. In this review, the strong interplay among topology, band structure and carrier mobility in recently discovered high carriers mobility topological semimetals is discussed and their effect on their magnetotransport properties is outlined. The huge magnetoresistance effect, especially in the Hall transverse configuration, and a new version of a three-dimensional quantum Hall effect observed in high-mobility Weyl and Dirac semimetals are reviewed. The design of novel quantum sensors based on solid-state semimetals is also encouraged.

Keywords: topological semimetals; band structure; magnetotransport properties; carrier mobility; magnetoresistance sensors

1. Introduction

Since the beginning of this century the investigation of the electrical transport properties of solid-state materials [1–3] has been a rapidly evolving field that has received a huge boost, especially after the discovery of graphene [4,5] and of its peculiar electrical transport and structural properties exhibited in different geometries (see e.g. [6–13]) as well as of materials displaying topologically protected electronic states.

Recently discovered and widely studied classes of topological materials are the topological insulators, i.e., topologically-protected materials characterized by a non-zero surface conductivity but preserving insulating properties in the bulk [14–16], and triple-point topological metals [17]. The concept of topological protection (and the interplay between topology and physics) has been extended to other types of materials featuring topological properties, with special regard to the novel class of topological semimetals, i.e., gapless semiconductors having linear dispersion bands in correspondence of the zero-gap points. Topological semimetals are represented by binary or ternary compounds [18–24] and are characterized by specific surface states [25,26]. In this respect, semimetals have been known since a long time in solid-state physics and materials science and their conduction features were attributed to pentavalent elements (such as arsenic, antimony, bismuth and to the graphite form of carbon [2,3]), though no topological properties were associated to these elements. One newly discovered class of 3D topological semimetals, the so called Weyl semimetals [27–39], are characterized by non-degenerate bands and encompass binary and ternary compounds that can be classified as type-I and type-II Weyl semimetals [22,23,40–42]. All of them exhibit massless excitations, the Weyl fermions [43], characterized by divergent Berry curvatures around the band crossing points. The topological charges are represented by Weyl points (or nodes) in the momentum space hosting monopoles. In turn, the flux of the Berry curvature [21] flows from one monopole to the other defining the unique topological properties of a topological semimetal which are strictly connected to its band structure [44,45]. An interesting physical consequence of the above described topological properties is that

Preprints (www.preprints.org) | NOT PEER-REVIEWED | Posted: 13 November 2023 doi:10.20944/preprints202311.0757.v1

Weyl nodes lead to peculiar topologically protected surface states, named topological Fermi arcs, able to connect bulk Weyl points with opposite chiralities [22,28,46–49]. Fang et al. [50] have also rigorously proved that multi-Weyl topological semimetals are stabilized by point group symmetry and can be regarded as new 3D topological semimetals. The counterpart of Weyl semimetals, characterized by doubly-degenerate bands, are 3D Dirac semimetals [40,51–56], which feature topological states with massless excitations, the Dirac fermions [57,58]. The bands of Dirac semimetals cross at the Dirac points on the Fermi surface, each of them fourfold degenerate and formed by the merging of a pair of Weyl points with opposite chiralities and thus characterized by a vanishing chiral charge or non-trivial Chern number [51,59–61]. Another recently discovered class of topological semimetals is the class of nodal-line semimetals [62–64] in which the conduction and the valence bands intersect at a circular line [22,65] and exhibit peculiar magneto-optical properties [66]. Also this class of semimetals is characterized by type-I and type-II nodal lines [67–69]. Recently, attention has been given to the understanding and calculation of semimetal topological invariants [70,71], as it was done for the other classes of topological materials.

The theoretical and numerical approaches together with solid-state computational methods developed to determine the band structure for other classes of materials have been recently applied also to topological semimetals. Examples are the nearly free electron model, the $\mathbf{k} \cdot \mathbf{p}$ perturbation theory [1,72], the tight-binding (TB) model [73] and the muffin-tin approximation (enabling to determine the energy bands of *d*-type transition metal atoms and insulators), the linear combination of atomic orbitals (LCAO) technique [74], the augmented-plane-wave (APW) method [75] (used to calculate the band energy of transition metals) and the *ab initio* total energy calculation using a plane-wave basis set [76,77]. The most frequently employed computational method, owing to its generality and simplicity, is the density functional theory (DFT) [78–81] together with its variations such as, e.g., the projected augmented-wave method (PAPW) [82], the linearized augmented-plane-wave (LAPW) method [83,84] (applied to periodic materials) and the full-potential linearized augmented-plane-wave method (FLAPW) (applied to any type of crystalline materials) [85]. These computational methods can be used for the determination of different types of bands (including those of semimetals) and allow to characterize solids in terms of their band structure and to understand how this latter affects velocity and mobility of electrons and holes.

The application of some of the abovementioned computational methods to the recently discovered topological semimetals [18,22,86] has allowed to understand the main differences among the structure of the energy bands of semimetals, graphene and III-V semiconductors. Semimetals are materials characterized by a small overlap between the bottom of the conduction band and the top of the valence band with electrical transport properties determined by two types of carriers, electrons and holes [22].

Semimetals can be regarded as metals but at the same time they inherit the transport properties of semiconductors. They are 3D phases of matter with gapless electronic excitations protected by symmetry and topology. Nearly ideal Dirac semimetals have been modeled by Tang et al.[87]. A Dirac semimetal phase with quantum transport origin has been observed in Cd_3As_2 [88], while a nontrivial Berry phase characterizes the layered material $PdTe_2$ [89] and type-II Dirac semimetals feature the YPd_2Sn class [90]. Examples of typical Weyl semimetals are single-crystal transition-metal monophosphides [91,92], magnetic compounds such as the canted antiferromagnet $YbMnBi_2$ [93], and the WTe_2 compound whose centrosymmetric phase [94] can coexist with topological insulators [95].

A crucial role in determining the electrical transport properties is played by carrier mobility $\mu_{e,h}$ with e (h) denoting electrons (holes). The carrier mobility expresses the velocity of an electric charge in a metal, semimetal or semiconductor under the effect of an applied electric field. It is proportional to the relaxation time and is inversely proportional to the effective mass, namely $\mu_e = \frac{e\tau}{m_e^*}$ for the electron mobility and $\mu_h = \frac{e\tau}{m_h^*}$ for the hole mobility, τ being the relaxation time (i.e., the characteristic time between two successive scattering events) and m_e^* (m_h^*) the electron (hole) effective mass. The mobility achieves its maximum value at low temperature because of the strong electron back-scattering protection (as occurs, e.g., in TaAs [96]), while it diminishes with increasing temperature [67,91,97,98]

 doi:10.20944/preprints202311.0757.v1

due to the enhanced scattering of electrons and holes with longitudinal acoustic and optical phonons occurring at intermediate and high temperatures and attains a minimum at room temperature, similar to semiconductors, graphene and graphite [72,99–101].

This review paper outlines the state-of-the-art of high-mobility topological semimetals and illustrates the recent advancements in the theoretical modeling and experimental measurement of the transport physical quantities, with special regard to mobility, electrical conductivity, magnetoresistance (MR) effect and a novel type of three-dimensional (3D) quantum Hall effect.

2. Band structure and electrical transport properties in high-mobility semimetals

The strict relationship among band structure, electronic properties and topology has a direct effect on the electrical properties of semimetals via the strong influence of the band curvature on carrier mobility and, in turn, on the electrical conductivity σ due to the proportionality between σ and carrier mobility. In perfect analogy with semiconductors [72,101], it is reasonable to suppose that the inverse of the electron effective mass m_e^* and of the hole effective mass m_h^* is proportional to the conduction and valence band curvature, respectively. At any temperature, the more the band curvature is accentuated, the larger are electron and hole mobilities μ_e and μ_h, and the semimetal electrical conductivity tends to increase (also depending on carrier concentrations).

In this respect, it is widely known that carrier mobility in several semimetals often exhibits high values [67,91,102]. Indeed, carrier mobilities in semimetals are much higher than those of electrons in metals and of electrons and holes in intrinsic and doped semiconductors and graphene. For "high-mobility" semimetals it is understood here that carrier mobility, of either electrons or holes, overcomes the 10^4 cm^2 V^{-1} s^{-1} threshold at temperatures close to $T = 0$ K and is not lower than 10^2 cm^2 V^{-1} s^{-1} close to room temperature. From this point of view, most topological semimetals fall into this category exhibiting unique and compelling magnetotransport properties [103,104] and the high mobility of their carriers leads to the observation of high electrical conductivity and huge MR even at low external magnetic fields. MR is defined as the change in electrical resistance due to an external magnetic field applied either perpendicular (Hall configuration) or parallel or forming an arbitrary angle with the direction of the electric current flowing in the material under study. At fixed external magnetic field, the MR strongly depends on carrier mobility and high-mobility semimetals are the ideal materials exhibiting huge and non-saturating MR even at low fields and at temperatures close to room temperature. The high MR value especially observed in the Hall configuration is an appealing feature to be exploited for the design of semimetal-based MR sensors which could offer advantages in terms of sensitivity and precision if compared to other types of solid-state sensors including graphene-based sensors.

2.1. Relation between topology and physics

The new classes of Dirac, Weyl and nodal-line semimetals originate from applications of the quantum relativistic theory to fermionic systems. Indeed, they can be regarded as solutions to Dirac and Weyl equations that are represented by Dirac and Weyl fermions [105,106].

Figure 1(a) shows that the conduction and valence bands of a Dirac semimetal match at a point lying on the Fermi surface, called Dirac point. This feature differs from the energy gap of a semiconductor, as illustrated in Figure 1(b). The 3D band structure of a Weyl semimetal displayed in Figure 1(c) shows the Weyl point, i.e., the matching point between electron and hole pockets on the Fermi surface. The Weyl point becomes a line in nodal-line semimetals (Figure 1 (d)). Figure 1(e) shows the Weyl point for a type-I Weyl semimetal, while Figure 1(f) illustrates the Weyl point typical of a type-II Weyl semimetal.

Preprints (www.preprints.org) | NOT PEER-REVIEWED | Posted: 13 November 2023 doi:10.20944/preprints202311.0757.v1

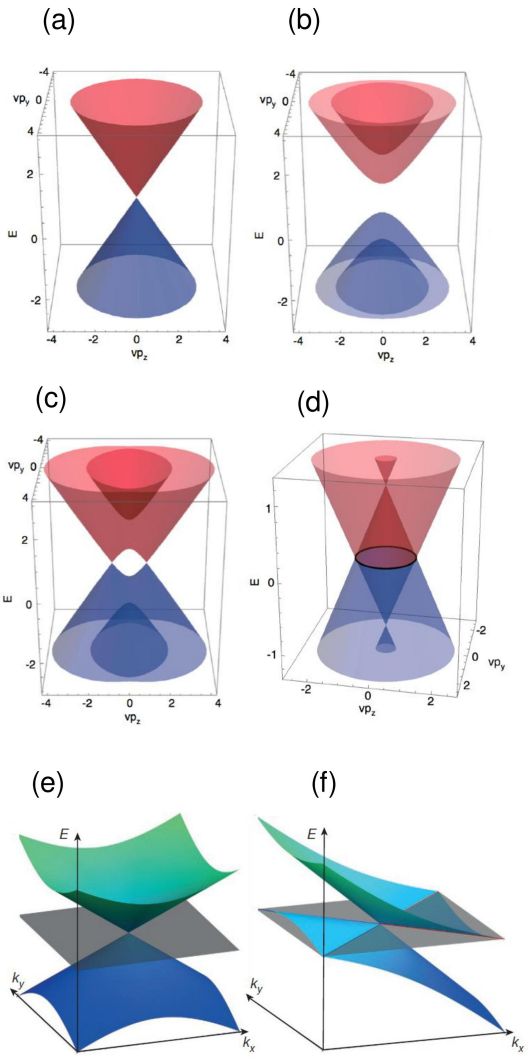

Figure 1. 3D representation of band diagrams. (a) Dirac semimetals. (b) Semiconductors. (c) Weyl semimetals. (d) Nodal-line semimetals (adapted from [22]). (e) Type-I Weyl point semimetal exhibiting a point-like Fermi surface. The Weyl point corresponds to the intersection point of the valence and conduction bands at the Fermi surface. (f) Type-II Weyl point semimetal corresponding to the contact point of electron and hole pockets (adapted from [23]).

Type-I and type-II Weyl semimetals [69,107–115] can be thought of as 3D phases of matter having electronic properties analogous to those of graphene and exhibiting gapless electronic excitations, the Weyl fermions, which are solutions to the Weyl equation in odd dimensions. Weyl fermions are protected not only by symmetry but also by topology and can possess also relativistic properties in the presence of a magnetic field [116]. On the other hand, Dirac semimetals exhibit similar features and arise from another type of gapless electronic excitations, the Dirac fermions, solutions to the Dirac equation.

Calculated band structures of some representative semimetals are displayed in Figure 2. Figure 2(a) shows the 3D bands of the NbP compound, a type-I Weyl semimetal [91,117] determined by DFT. The intersection of the Fermi level with the valence band has an effect on carrier mobility and electrical conductivity, which noticeably increase due to a larger contribution from holes populating the valence band if compared to the contribution resulting from electrons in the conduction band. In turn, also the MR becomes extremely large even at room temperature for rather high transverse magnetic fields.

Preprints (www.preprints.org) | NOT PEER-REVIEWED | Posted: 13 November 2023 doi:10.20944/preprints202311.0757.v1

Figure 2(b) [118,119] displays the bands of the type-II Weyl semimetal WTe_2. The calculated band structure of the Dirac semimetal $LaAgSb_2$ is shown in Figure 2(c) [120], while Figure 2(d) illustrates the band structure of a CaTe mixed nodal-line and Dirac semimetal [65].

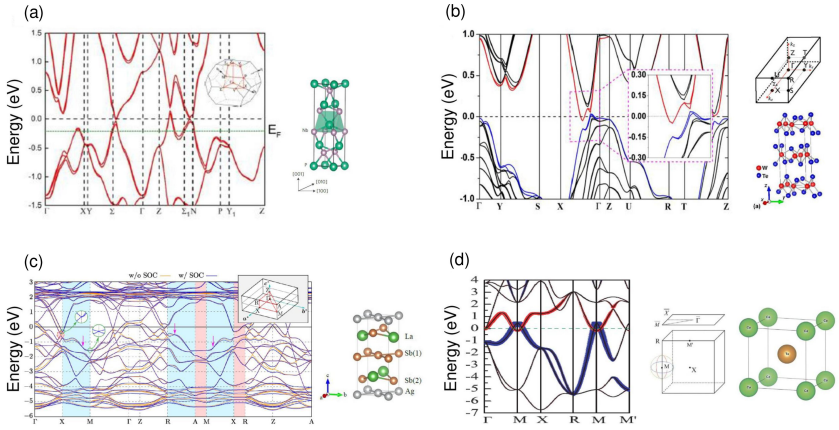

Figure 2. (a) Calculated band structure of type-I Weyl semimetal NbP together with its 3D Brillouin zone. The Fermi level intersects the valence band. The NbP tetragonal Bravais lattice is shown (adapted from [91,117]). (b) Calculated band structure of type-II Weyl semimetal WTe_2. The 3D Brillouin zone and the orthorombic Bravais lattice are displayed (each Tungsten layer is sandwiched between two Tellurium layers with strong ionic bonds (adapted from [118,119]). (c) Calculated band structure of $LaAgSb_2$ Dirac semimetal together with the 3D Brillouin zone. The tetragonal lattice is depicted (adapted from [120]). (d) Band structure without spin-orbit coupling of the CaTe mixed nodal-line and Dirac semimetal in CsCl-type phase. The 3D Brillouin zone projected on the plane and the bcc lattice are shown (adapted from [65]).

Experimentally, the band structure of semimetals can be reconstructed by means of angle-resolved photoemission spectroscopy (ARPES), a technique allowing to probe their surface states [91,121]. Instead, powder X-ray diffraction and single-crystal X-ray diffraction are the most widely used experimental techniques to investigate the structural and lattice properties of high-mobility semimetals [91].

2.2. Electrical transport properties: carrier mobility and electrical conductivity

The calculation of the band structure of high-mobility semimetals is pivotal for the full understanding of their electrical properties, particularly the electron and hole mobility and, in turn, their corresponding electrical conductivities and their dependence on temperature T, analogously to what happens for intrinsic as well as doped semiconductors [122].

It is reasonable to suppose that, also for topological semimetals, carrier mobility is inversely proportional to the carrier effective mass, i.e., $\mu_e(\mu_h) \propto 1/m_e(1/m_h)$, which, in turn, depends on the curvature of the bands, namely $1/m_e \propto \partial^2 E_c/dk^2$ ($1/m_h \propto \partial^2 E_v/dk^2$), where E_c (E_v) is the conduction (valence) band energy [101]. The effective mass of electrons is generally much lower than that of holes, leading to a lower mobility of the latter. However, due to the peculiar band structure of semimetals for which the Fermi level intersects the valence band, holes also play a key role in the electrical transport properties and could give an appreciable contribution to the total conductivity. The most investigated topological semimetals so far have been the Weyl I semimetals for their peculiar transport properties. The Hall coefficient $R_H(T)$, calculated from the slope of the measured off-diagonal component of the resistivity ρ_{xy} is negative in the range $0\,\mathrm{K} < T < 125\,\mathrm{K}$ and positive for $125\,\mathrm{K} < T \leq 300\,\mathrm{K}$. Carrier mobility can be extracted from the Hall coefficient $R_H(T)$ applying to Weyl semimetals a single-band

Preprints (www.preprints.org) | NOT PEER-REVIEWED | Posted: 13 November 2023 doi:10.20944/preprints202311.0757.v1

Drude model, namely $\mu_{e,h} = R_H(T)/\rho_{xx}$, ρ_{xx} being the diagonal component of the resistivity tensor and $R_H(T)$ a function of the electron (hole) density $n_e(T)(n_h(T))$.

In Figure 3 the measured electron and hole mobility dependence on temperature is displayed for four topological semimetals belonging to different classes. Even though the quantitative values may differ depending on the chosen semimetal for each class, the trends reported here can be considered general. Measurements of carrier mobility in the Cd_3As_2 Dirac semimetal are available only for $0 < T \leq 150$ K. At temperatures close to $T = 0$ K, the NbP Weyl-I semimetal (Figure 3(a)) exhibits the highest electron and hole mobility values, while, at room temperature, the measured carrier mobility is higher in the CaAgP nodal-line semimetal (about 10^4 cm$^2\cdot$ V$^{-1}\cdot$ s^{-1}), although in this case the measurement was performed by doping the semimetal with Pd atoms. The undoped hole mobility in the CaAgP nodal-line Dirac semimetal is almost independent of T and of the order of 10^3 cm$^2\cdot$ V$^{-1}\cdot$ s^{-1} for the whole $0 < T \leq 200$ K range. The MoP type-II Weyl semimetal exhibits the lowest carrier mobility (Figure 3(b)) if compared to the measured mobilities of carriers in other representative semimetals. This dissimilar behavior is related to the profound differences in the band curvatures of the various semimetals. Valence and conduction bands in NbP feature a higher curvature than those of other semimetals, which results in a dramatic increase of electron and hole mobility (especially at low temperatures). On the other hand, the smaller band curvature of MoP results in a more than two orders of magnitude lower carrier mobility than that of NbP.

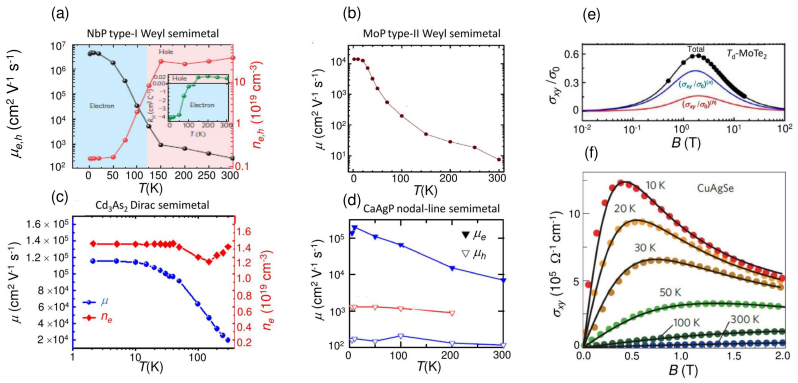

Figure 3. Measured temperature-dependent mobility, carrier density and electrical conductivity of representative topological semimetals. The mobility and the carrier density were extracted from Hall resistivity and Hall coefficient measurements. (a) Black line with circles: NbP type-I Weyl semimetal electron and hole mobility vs. T for $0 < T \leq 300$ K. Red lines with circles: carrier density vs. temperature for $0 < T \leq 300$ K. In the inset the dependence of the Hall coefficient on temperature T is also shown (adapted from [91]). (b) Carrier mobility in the MoP type-II Weyl semimetal vs. T (adapted from [97]). (c) Blue line with full circles: carrier mobility in the Cd_3As_2 Dirac semimetal as a function of temperature T for $0 < T \leq 150$ K extracted from a Hall measurement. Red line with diamonds: electron carrier density vs. T (adapted from [98]). (d) Red line with empty down-triangles: hole carrier mobility in the undoped CaAgP nodal-line semimetal vs. T. Blue line with empty down-triangles: hole carrier mobility in the Pd-doped CaAgP nodal-line semimetal vs. T. Blue line with full down-triangles: electron carrier mobility in the Pd-doped CaAgP nodal-line semimetal vs. T (adapted from [67]). (e) Measured transverse electrical conductivity of T_d-$MoTe_2$ type-I Weyl semimetal expressed in normalized units as a function of the applied magnetic field at $T = 2$ K. Red curve: contribution of the holes to the electrical conductivity. Blue curve: contribution of the electrons to the electrical conductivity. Black curve: total normalized electrical conductivity (adapted from [123]). (f) Measured transverse conductivity of CuAgSe Dirac semimetal as a function of the applied magnetic field at different temperatures (adapted from [124]).

Preprints (www.preprints.org) | NOT PEER-REVIEWED | Posted: 13 November 2023 doi:10.20944/preprints202311.0757.v1

In this respect, the NbP compound can be regarded as a promising very high-mobility material because it incorporates the main transport features of the WTe_2 type-II Weyl semimetal and the ones of the Cd_3As_2 Dirac semimetal (whose carrier mobility is shown in Figure 3(c)). The NbP carrier mobility reaches a maximum value of about 5×10^6 cm$^2\cdot$ V$^{-1}\cdot$ s^{-1} at $T = 1.5$ K allowing to consider NbP a ultra-high mobility semimetal. The trend of carrier density ($n_{e,h}$) as a function of T is very different passing from a type-I Weyl semimetal to a Dirac semimetal. By comparing the NbP electron and hole density with Cd_3As_2 electron density, it can be observed that the former dramatically increases with T due to a strong contribution from holes at intermediate and high temperatures close to room temperature, while the latter is almost independent of T showing a dip at $T \simeq 130$ K, and its value is one order of magnitude smaller than $n_{e,h}$ of NbP (which includes also the hole contribution). Hall resistivity measurements allow to separate the electron and hole mobility in the CaAgP nodal-line semimetal shown in Figure 3d. The Pd-doped CaAgP is a high-mobility semimetal and especially electron mobility attains a maximum at T close to 0 K with $\mu_e > 10^5$ cm$^2\cdot$ V$^{-1}\cdot$ s^{-1}.

Figure 3(e) and (f) show the behavior of the measured transverse conductivity (σ_{xy}) vs. B for the T_d-$MoTe_2$ type-I Weyl semimetal and for the CuAgSe Dirac semimetal. Up to $T = 50$ K, the transverse conductivity σ_{xy} attains a maximum for both electrons and holes and then it decreases with B reproducing the trend given in Eq.3 (see next section). The maximum of σ_{xy} shifts towards higher values of B and decreases with increasing T. This trend confirms that, at fixed B, electron and hole conductivities diminish with increasing T due to the reduction of their respective mobilities, ultimately caused by the strong scattering with longitudinal acoustic and optical phonons and with lattice impurities.

3. High-mobility semimetals and magnetotransport properties

To determine the relationship between the electronic properties and the magnetotransport properties of all types of topological semimetals it is crucial to quantify the MR effect, a physical phenomenon observed in different types of materials consisting in the change of electrical resistance due to the application of an external magnetic field of magnitude B. Another relevant physical phenomenon recently discovered in some types of semimetals which is also related to the electronic properties is the 3D version of the quantum Hall effect [125] generally observed in two-dimensional (2D) systems. In the following subsections, these two effects (strictly dependent on the high-mobility properties of the topological semimetals) are reviewed and some applications thereof are discussed.

3.1. Magnetoresistance effect: theoretical framework and applications

The MR can be measured in different geometric configurations determined by the relative angle between the electric current I and the magnetic field $\mathbf{B}$. Also for the case of semimetals the most common MR measurement is performed in the Hall configuration with $\mathbf{B}$ oriented out-of-plane and perpendicular to the direction of the current. The main source of MR in semimetals is related to the deviation of the charge carrier (both electrons and holes) trajectory due to the Lorentz force (Hall effect). During the last years, great attention has been devoted to the MR effect in high-mobility semimetals and it has been found that topological semimetals exhibit a huge MR effect [126–133] as occurs for topological insulators [134]. Quantitatively, and analogously to other types of materials, the MR can be expressed also for topological semimetals in percentage units as:

$$\mathrm{MR}(\%) = \left(\frac{\rho(B) - \rho(0)}{\rho(0)}\right) \times 100\%, \tag{1}$$

where $\rho(B)$ is the material electrical resistivity at $B \neq 0$ T and $\rho(0)$ is the material electrical resistivity at $B = 0$ T, i.e., $\rho(0) = \rho_0$ (expressed in Ω m or Ω cm). For both electrons and holes ($i = e, h$),

Preprints (www.preprints.org) | NOT PEER-REVIEWED | Posted: 13 November 2023 doi:10.20944/preprints202311.0757.v1

the field-dependent electrical resistivity $\rho(B)$ and electrical conductivity $\sigma(B) = 1/\rho(B)$ at low and intermediate magnetic fields can be written as [135]:

$$\rho = \rho_0 \begin{pmatrix} 1 & \mu_i B \\ -\mu_i B & 1 \end{pmatrix} \tag{2}$$

$$\sigma = \frac{\sigma_0}{1 + (\mu_i B)^2} \begin{pmatrix} 1 & -\mu_i B \\ \mu_i B & 1 \end{pmatrix} \tag{3}$$

with $\sigma_0 = \sigma(0)$ the electrical conductivity at $B = 0$ T. Specifically, for fixed mobility μ_i, at low B the conductivity $\sigma_{xy} \propto \mu_i B$, namely it linearly increases with the external magnetic field, while at intermediate and high fields $\sigma_{xy} \propto 1/(\mu_i B)$, i.e., the electrical conductivity rapidly diminishes with increasing B.

The MR is, in general, huge even for small external magnetic fields in high-mobility semimetals especially at low temperatures at which the carrier mobility and the electrical conductivity are remarkable. Topological semimetals, both of the Dirac and Weyl type, show high MR due to a balanced hole-electron resonance effect resulting from their peculiar band structure, therefore there is not only the contribution to MR from electrons but also from holes. As a consequence, the MR does not saturate at low and intermediate B, as occurs for semiconductors and graphene.

In Figure 4 the general trend of measured MR for some representative topological semimetals is displayed. Figure 4(a) graphically expresses the relationship between the measured MR (%) and electrical conductivity σ_0. This dependence is shown for MR (%) probed at $T = 2$ K and at $B = 9$ T [126]. The highest MR(%) (almost 10^7) is measured in WP_2 (a Weyl II semimetal) at a conductivity of about $10^9\ \Omega^{-1}\ cm^{-1}$ and a slightly lower value is exhibited by MoP_2, another Weyl II semimetal. However, also NbP, LaSb and $PtBi_2$, which are Weyl I semimetals, exhibit a MR (%) of about 10^6 at lower conductivities. Lower but still considerable values of MR (%) (about 10^5) are typical of TaAs, the transition-metal dichalcogenides WTe_2, $NbSb_2$, $PtSn_4$ representing Dirac nodal semimetals and the Cd_3As_2 Dirac semimetal.

It is well-known that MR is proportional to resistivity but is inversely proportional to conductivity so that the MR effect is significant in low-conductivity materials. However, looking at Figure 4(a), Weyl II semimetals WP_2 and MoP_2 simultaneously exhibit large MR and high values of conductivity larger than those of the Cd_3As_2 Dirac semimetal and with σ of the same order of magnitude as K and one order of magnitude smaller than Cu. Therefore, Weyl II semimetals are materials having large carrier mobilities comparable to those of the typical metals. This means that they can be regarded as materials very similar to metals and with electrical transport properties not only determined by electrons but also by holes.

Figure 4(b-e) display MR measurements of typical high-mobility semimetals as a function of the applied external magnetic field at different temperatures in the Hall configuration, i.e. the out-of-plane external magnetic field $\mathbf{B}$ is perpendicular to the in-plane current ($\theta = 90^0$). The two general observations for all the semimetals, which can be drawn looking at Figure 4(b-e), are: 1) MR does not reach a saturation value but tends to increase with increasing B for low and intermediate B and 2) MR decreases with increasing T as in III-V semiconductors but at room temperature it is still huge. Regarding 1), the contribution to MR due to holes in high-mobility semimetals is more relevant with respect to the one present in III-V semiconductors giving rise to a more accentuated electron-hole resonance effect which leads to a larger MR value in semimetals.

Preprints (www.preprints.org) | NOT PEER-REVIEWED | Posted: 13 November 2023 doi:10.20944/preprints202311.0757.v1

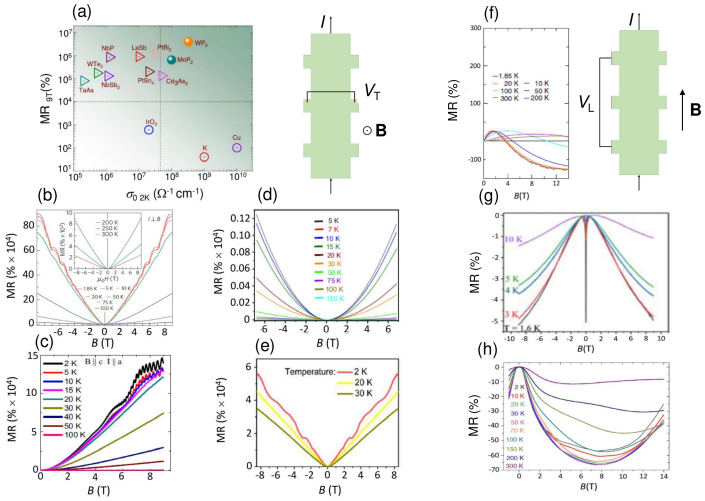

Figure 4. (a) Observed MR at $B = 9$ T as a function of the electrical conductivity for a temperature $T = 2$ K for representative topological semimetals in the Hall configuration. Triangles: Weyl I semimetals and Dirac semimetals. Full circles: Weyl II semimetals. As a comparison, the MR of metals, K, and Cu, together with that of a metal oxide, IrO_2, (hollow circles) are also depicted (adapted from [126]). MR (%) of some representative different types of semimetals measured in the Hall configuration ($\mathbf{B} \perp I$) at different temperatures with $\mathbf{B}$, the out-of-plane external magnetic field for(b) a NbP type I Weyl semimetal (adapted from [91]); (c) a WTe_2 type II Weyl semimetal (adapted from [132]); (d) a ZrSiS Dirac semimetal (adapted from [133]); (e) a ZrGeSe nodal-line semimetal (adapted from [136]). The geometry corresponding to the Hall MR configuration ($\mathbf{B} \perp I$) with V_T the transverse potential is also displayed. MR (%) of some representative different types of semimetals measured in the longitudinal configuration ($\mathbf{B} \parallel I$) at different temperatures with $\mathbf{B}$, the in-plane external magnetic field for (f) a TaP type-I Weyl semimetal (adapted from [137]); (g) a $TaAs_2$ type-II Weyl semimetal transitioning from the topological insulator state as soon an external magnetic field is applied (adapted from [121]); (h) a Cd_3As_2 Dirac semimetal (adapted from [44]). The geometry corresponding to the longitudinal MR configuration ($\mathbf{B} \parallel I$) with V_L the longitudinal potential is also shown.

Concerning 2), also in high-mobility semimetals carrier mobility decreases with increasing temperature due to the huge scattering of electrons and holes with acoustic and optical phonons, especially at intermediate and high T close to room temperature, but the effect of scattering is partially masked by the appreciable contribution of holes to the mobility. One notes that there are some quantitative discrepancies among the measured MR (%) values depending on the type of semimetal. In particular, the highest values at any temperature are exhibited by the NbP type-I Weyl semimetal, but also the WTe_2 type-II Weyl semimetal shows big values of MR(%) especially at large applied external magnetic fields. On the other hand, at fixed external magnetic field, the MR (%) for the representative Dirac semimetal is at least one order of magnitude less than the one exhibited by Weyl semimetals, while the nodal-line semimetal has a MR (%) comparable to the one of type II Weyl semimetal. The reason of these discrepancies is attributed to the higher carrier mobility characterizing Weyl semimetals which leads to a more accentuated increase of the field-dependent resistivity with increasing B as expressed by Eq. (2).

MR is measured also for other geometries ($0 < \theta < 90^o$) and in the so-called longitudinal configuration with $\mathbf{B} \parallel I$. As shown in Figure 4(f-h) [107,121,137,138] the MR vs. $\mathbf{B}$ is negative and the minimum deepens with decreasing T. When $\mathbf{B}$ is not orthogonal to the current (and, as a result, to the electric field $\mathbf{E}$) there is not anymore the quantum mechanical conservation of the particle number, the so called Adler–Bell–Jackiw anomaly or chiral anomaly which manifests itself in the presence of well-defined chirality appearing when the Fermi level is close to the Weyl nodes [137]. It can be proved that chiral anomaly in Weyl semimetals leads to negative MR vs. $\mathbf{B}$ with MR absolute value increasing as temperature decreases and this effect is maximum when $\mathbf{B} \parallel \mathbf{E}$. In the presence of chiral anomaly,

Preprints (www.preprints.org) | NOT PEER-REVIEWED | Posted: 13 November 2023 doi:10.20944/preprints202311.0757.v1

the external magnetic field suppresses the phase coherence of the back-scattered electron and hole waves and destroys the weak localization effect. The more **B** deviates from the collinear configuration with the current, the more the Lorentz force gives a positive contribution which cancels the negative MR effect.

Considering that the MR absolute value is much lower with respect to that in the Hall configuration at fixed B intensity, the design of MR sensors based on this effect could be useful but less exploitable if compared to that in the Hall geometry.

The mobilities of representative topological semimetals are summarized in Table 1 together with their MR(%) at low temperatures and at given values of the external magnetic fields [20]. Among the different types of semimetals, Weyl II semimetals are the ones exhibiting the highest MR(%) but also Weyl I semimetals are characterized by high mobility especially at low temperature and, as a result, also by a huge value of MR(%). Looking at Table(1) one notes that there is a strict relationship between the two physical quantities as for other types of high-mobility materials such as graphene or some types of III-V semiconductors.

Table 1. Carrier mobilities, conductivities and MR obtained in the transverse Hall configuration for various applied magnetic fields of a few representative topological semimetals.

Semimetal	Mobility $\mu_{e,h}$ ($cm^2 \cdot V^{-1} \cdot s^{-1}$)	Resistivity ρ_0 ($\Omega \cdot$ cm)	MR (%)
NbP [91]	5×10^6 (1.85K)	6.3×10^{-9} (2 K)	8.5×10^5 (1.85K, 9T)
$NbSb_2$ [139,140]	2.1×10^4 (5K)	8×10^{-9} (2K)	1.3×10^5 (2K, 9T)
NbAs [141]	3.5×10^5 (2K)	1×10^{-8} (2K)	2.3×10^5 (2K, 9T)
TaP [117,142,143]	3×10^5 (2K)	4×10^{-6} (2.5 K)	2.31×10^4 (5K, 6T)
TaAs [96]	5×10^5 (2K)	1×10^{-6} (1K)	5.4×10^5 (10K, 9T)
WP_2 [126]	4×10^6 (2K)	3×10^{-9} (2K)	4.2×10^6 (2K, 9T)
WTe_2 [130,144]	5.0×10^3 (1.6K)	1.9×10^{-6} (2K)	4.5×10^5 (4.5K, 14.7 T)
$PtSn_4$ [145,146]	1×10^5 (2K)	4×10^{-8} (2K)	5×10^5 (1.8K, 14T)
$PtBi_2$ [147]	3.1×10^4 (2K)	2.4×10^{-8} (2K)	1.12×10^7 (1.8K, 33T)
Cd_3As_2 [128]	9×10^6 (5K)	2×10^{-5} (2K)	3.1×10^3 (2K, 9T)
MoP_2 [126]	4×10^6 (2K)	1×10^{-8} (2K)	3.2×10^5 (2K, 9T)
MoP [97]	1×10^4 (2K)	6×10^{-9} (2K)	3.2×10^3 (2K, 14T)

3.2. Novel type of quantum Hall effect in 3D topological semimetals

Very recently, a 3D quantum Hall effect has been reported in some types of high-mobility topological semimetals [125,148,149]. It can be considered the equivalent in three dimensions [150] of the usual 2D quantum Hall effect [151,152]. This effect, also called integer quantum Hall effect to distinguish it from the fractional quantum Hall effect, is the corresponding quantum version of the Hall effect. It consists of the quantization of the Hall conductance (or equivalently of the Hall resistance) in 2D (x-y plane) electron systems brought to low temperature (liquid helium temperature $T = 4.2$ K) in the presence of a strong external magnetic field B (several Tesla) applied perpendicularly to the plane of the charge carrier system. The Hall quantized electrical conductance $G_H = I/V_{Hall}$ with I the electrical current and V_{Hall} the Hall potential can be expressed as $G_H^{2D} = \frac{n e^2}{h}$, where $n = 1, 2, ...$ is a non-negative integer expressing the G_H^{2D} quantization in terms of Landau levels lying below the Fermi energy E_F, e is the electron charge and h is the Planck constant. In 2D systems G_H^{2D} has the dimensions of e^2/h in Siemens (S), while in 3D systems G_H^{3D} has the dimensions of e^2/h over length in S/m or S/cm.

The main observed feature is the exhibition of the quantum Hall conductance plateaus at $\frac{e^2}{h}, \frac{2e^2}{h}, ...$ either as a function of $1/B$ or of the carrier density which persist by varying widely B or the carrier density. Equivalently, the quantum Hall resistance $|R_{xy}| = \frac{h}{n e^2}$ shows plateaus at $\frac{h}{e^2}, \frac{h}{2e^2}, ...$) as a function of B or of the electron density. This result looks surprising because quantum Hall conductance

Preprints (www.preprints.org) | NOT PEER-REVIEWED | Posted: 13 November 2023 doi:10.20944/preprints202311.0757.v1

does not depend explicitly on carrier density. The family of TaAs Weyl semimetals together with the Cd_3As_2 and Na_3Bi Dirac semimetals are high-mobility materials and, therefore, satisfy the main requirement necessary to exhibit the 3D quantum Hall effect. The main requirement is the presence of the Fermi arcs placed on the Fermi surface between Weyl nodes and formed by the topologically protected states. In this way, by exploiting the tunnel effect, the electrons can pass through the Fermi arcs placed at opposite surfaces via a "wormhole" tunneling supported by the Weyl nodes [125]. In addition, to have the 3D quantum Hall effect: 1) the Fermi arcs should also make closed Fermi loops; 2) bulk carriers must be depleted by tuning the Fermi energy to the Weyl nodes and 3) there should be band anisotropy so that the Fermi arcs give rise to a 2D gas [125]. Due to the time-reversal symmetry, a complete Fermi loop representing one of the requirements to observe a 3D quantum Hall effect occurs on a single surface of the Cd_3As_2 and Na_3Bi Dirac semimetals. In particular, the 3D quantum Hall effect based on Weyl orbits has been recently realized in the 3D Dirac Cd_3As_2 high-mobility semimetal in nanostructured form [149]. It is crucial to understand the behavior of Weyl orbit under an external magnetic field. There are two pairs of Weyl nodes of opposite chiralities acting like "wormholes" connected by Fermi arcs lying on two opposite surfaces in the k_x-k_z plane, the top and the bottom Fermi arc. The propagation of the electrons occurs along the z-direction through the bulk chiral Landau levels in order to complete the cyclotron motion.

The quantized 3D Hall conductivity for topological Weyl and Dirac semimetals can be calculated starting from the Kubo formula

$$\sigma_{\mathrm{H}}^{3\mathrm{D}\,sm} = \frac{e^2\hbar}{iV_{\mathrm{eff}}} \sum_{\delta,\delta'\neq\delta} \frac{\langle\Psi_\delta|v_x|\Psi_{\delta'}\rangle\,\langle\Psi_{\delta'}|v_z|\Psi_\delta\rangle\,\big(f(E_{\delta'})-f(E_\delta)\big)}{(E_\delta-E_{\delta'})(E_\delta-E'_\delta+i\Gamma)} \tag{4}$$

with sm = Weyl, Dirac, Ψ_δ the eigenstate corresponding to the energy E_δ when the external magnetic field is applied along the y direction, v_α with $\alpha = x,z$ the velocity operator, $f(E_\delta)$ is the Fermi distribution, V_{eff} the effective volume of the slab or the areas hosting the Fermi arcs and Γ expresses the level broadening. $\Gamma \to 0$ means that disorder is weak and does not affect the width of plateaus. The sheet 2D quantum Hall conductivity having dimensions of e^2/h (S) is obtained as $\sigma_{\mathrm{H}}^{\mathrm{S}\,s} = \sigma_{\mathrm{H}}^{3\mathrm{D}\,s}L$ with L the slab thickness. First, let's deal with the quantum Hall conductivity $\sigma_{\mathrm{H}} = J_x/E_z$ (with the current density along x and the induced electric field along z) of the Weyl topological semimetal. From Eq. (4) it turns out to be at zero temperature[125]

$$\sigma_{\mathrm{H}}^{3\mathrm{D\,Weyl}} = t\frac{e^2}{h}\frac{4}{Ll_B^4} \sum_{E_\delta<E_F,E_{\delta'}>E_F} \frac{\mathrm{Re}(\bar{v}_x^{\delta\delta'}\bar{v}_z^{\delta'\delta})}{(E_\delta-E_{\delta'})^2+\Gamma^2} \tag{5}$$

with $t = \mathrm{sgn}(eB)$, $l_B = \sqrt{\hbar/|eB|}$, $\bar{v}_x^{\delta\delta'}\delta_{k'_x,k_x} = \hbar\frac{l_B}{\sqrt{2}}\langle\Psi_\delta|v_x|\Psi_{\delta'}\rangle$,
$\bar{v}_z^{\delta'\delta}\delta_{k'_x,k_x} = \hbar\frac{l_B}{it\sqrt{2}}\langle\Psi_{\delta'}|v_z|\Psi_\delta\rangle$ and $\sigma_{\mathrm{H}}^{\mathrm{S\,Weyl}} = \sigma_{\mathrm{H}}^{3\mathrm{D\,Weyl}}L$.

Let's now calculate the quantum Hall conductance of Fermi arc I at the upper slab surface ($y = L/2$). The effective Hamiltonian of the Fermi arc in a 3D Weyl topological semimetal having the form of a slab of thickness L (see Figure 5) can be derived from the Hamiltonian of a 3D Weyl topological semimetal and parametrized in the form $H_{\mathrm{arc}} = D_1k_w^2 + vk_x + (D_2-D_1)(k_x^2+k_z^2)$ for the $y = L/2$ surface with $v = A\sqrt{M^2-D_1^2}/M$ being D_1, D_2, A and M model parameters. The quantum Hall conductance of arc I $G_{\mathrm{H}}^{\mathrm{arc}}$ for a Weyl topological semimetal slab (for $\Gamma \to 0$) obtained from the 2D electron gas quantum Hall conductivity $\sigma_{\mathrm{H}} = ne^2/h$ (with $n = 1,2,..$ the number of Landau levels below the Fermi energy) is [125]

$$G_{\mathrm{H}}^{\mathrm{arc\,Weyl}} = \frac{e^2}{h}\,\mathrm{sgn}(R)\,\mathrm{sgn}(eB)\left\lfloor\frac{S_{\mathrm{I}}/(2\pi)^2}{eB/h}+\frac{1}{2}\right\rfloor \tag{6}$$

with $R = D_2 - D_1$, $S_{\mathrm{I}} = 2k_w^2(1+v^2/4R^2k_w^2\arctan(2|R|k_w/|v|) - |v|k_w/|R|$ the area filled by arc I in the momentum space and $\lfloor...\rfloor$ denoting rounding down. The sign of the quantum Hall conductance

Preprints (www.preprints.org) | NOT PEER-REVIEWED | Posted: 13 November 2023 doi:10.20944/preprints202311.0757.v1

depends on the signs of R and of eB in turn depending on the carrier type, charge type and on the direction of the external magnetic field. Similar conclusions can be drawn by considering Fermi arc II at the lower slab surface ($y = -L/2$).

Analogously, also the quantum Hall conductivity of a Dirac semimetal slab can be calculated from (4) at zero temperature. It turns out to be [125]

$$\sigma_{\mathrm{H}}^{\mathrm{Dirac}} = \frac{e^2}{h}\frac{8\pi t_y}{V l_y^2}\sum_{k_x'}\sum_{E_\delta<E_F, E_{\delta'}>E_F}\frac{\mathrm{Re}(\bar{v}_x^{\delta\delta'}\bar{v}_z^{\delta'\delta})}{(E_\delta - E_\delta')^2+\Gamma^2} \tag{7}$$

with $t_y = \mathrm{sgn}(eB_y)$, $l_y = \sqrt{\hbar/|eB_y|}$ being $\mathbf{B} = (B_x, B_y, 0)$ the uniform magnetic field applied in the x'-y' plane, V volume of the slab, $k_x' = k_x\sqrt{m_z/m_x}$ being k_x the x-component of the wave vector, m_x and m_z the effective masses of the electrons, $\bar{v}_x^{\delta\delta'}\delta_{k_x'',k_x'} = \hbar\frac{l_y}{\sqrt{2}}\langle\Psi_\delta|v_x|\Psi_{\delta'}\rangle$, $\bar{v}_z^{\delta'\delta}\delta_{k_x'',k_x'} = \hbar\frac{l_y}{it_y\sqrt{2}}\langle\Psi_{\delta'}|v_z|\Psi_\delta\rangle$.

Figure 5 shows the 3D quantum Hall effect observed both in the TaAs family topological Weyl semimetal (5 (a)-(d)) and in the Cd_3As_2 topological Dirac semimetal ((5 (e)-(l))). Figure 5(a)-(b) display the topological features of 3D TaAs in the form of a slab occurring in the presence of a 3D quantum Hall effect including the energy dispersion and the topology of the Fermi arcs at $E_F = E_w$. In Figure 5(c) the corresponding calculated 2D sheet quantum Hall conductivity vs. the inverse of the magnetic field shows the distinctive plateaus expression of the Landau level quantization of Hall conductivity. An analogous behavior is depicted in Figure 5(d) for the quantum Hall conductance of Fermi arc I.

In Figure 5(e)-(h) the behaviors of the measured longitudinal resistance R_{xx} and of the transverse Hall resistance $-R_{yx}$ of Cd_3As_2 films lying on the $x-y$ plane of different thicknesses as a function of the magnetic field B are shown. All films are characterized by the same carrier density $n = 1\times10^{18}$ cm^{-3}. As soon as the external magnetic field is turned on, Shubnikov-de Haas (SdH) oscillations of the longitudinal resistance begin to appear exhibiting a decreasing frequency with increasing the magnitude of the magnetic field. The vanishing of R_{xx} occurs for $B = 35$ T, especially for the smaller thicknesses (Figure 5(g) and (h)).

By observing the trend of the transverse Hall resistance $-R_{yx}$, the quantum Hall states begin to appear analogously to what occurs for the calculated conductivity. In the special case, the quantized values can be expressed in the form $\frac{1}{R_{yx}} = -\nu\frac{e^2}{h}$, with $\nu = s\,n$ an integer number depending in this case not only on $n = 1, 2, ..$ but also on the degeneracy factor s. One notes that the integer quantum Hall states clearly emerge for $\nu = 2$ for all the thicknesses considered. Moreover, the degeneracy factor drastically changes from $s = 2$ to $s = 1$ for the thickness passing from $t = 14$ nm to $t = 16$ nm. This change is due to spin splitting and is not related to other types of degeneracies, such as the lifting of valley or surface states. Interestingly, by performing the Fourier transform of the SdH oscillations the area A_{F} of the Fermi surface can be calculated via the Onsager relation as $A_{\mathrm{F}} = 4\pi e/h\, B_{\mathrm{F},1}$ where $B_{\mathrm{F},1}$ is the primary oscillation frequency. For example, for the $t = 12$ nm film $A_{\mathrm{F}} = 3.3\times10^{-3}$Å^{-2}.

Figure 5(i) illustrates the 3D quantum Hall modelization for a Cd_3As_2 slab (coordinate system x'-y'-z') grown along the [112] and [110] crystallographic directions and the corresponding calculated sheet Hall conductivity as a function of $1/B_y'$ for different orientations of the magnetic field marked by the angle ξ for $E_F = E_w$ (Figure 5(l)). Conductivity plateaus appear for any orientation of $\mathbf{B}$ and their widths are of different sizes for any χ investigated.

Preprints (www.preprints.org) | NOT PEER-REVIEWED | Posted: 13 November 2023 doi:10.20944/preprints202311.0757.v1

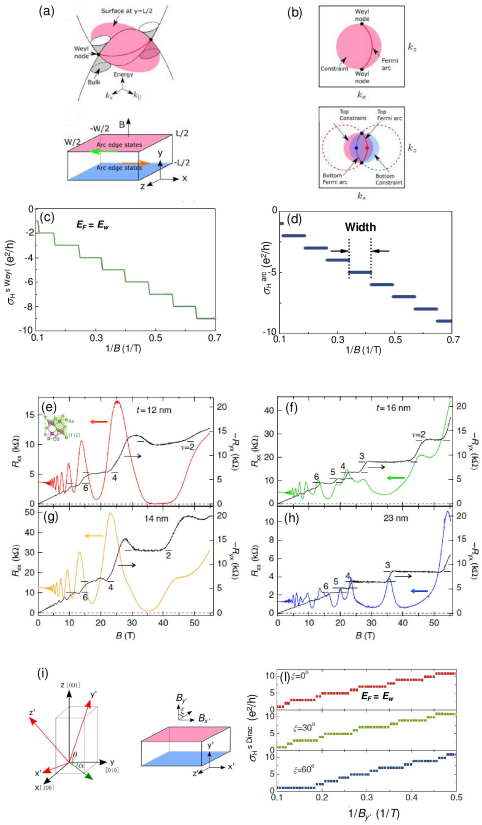

Figure 5. (a) Energy dispersion of a topological Weyl semimetal (e.g. TaAs family) and the slab of thickness L and width W. **B** is applied along the y direction. (b) Sketch of the Fermi arc at $y = L/2$ and $E_F = E_w$. The Fermi arcs can exist on the shadow area. The top (solid red line) and bottom (solid blue line) Fermi arcs at the $y = L/2$ and $y = -L/2$ surfaces of the slab at $E_F = E_w$ and the corresponding top and bottom constraints (pink shadow and cyan shadow areas). (c) The sheet quantum Hall conductivity for the slab of a topological Weyl semimetal calculated by means of Eq.(5) for $E_F = E_w$ where E_F crosses the arc I. (d) Calculated quantum Hall conductance for of arc I $G_{\mathrm{H}}^{\mathrm{arc}}$ of a Weyl semimetal according to Eq.(6). Adapted from [125]. (e)-(h) Measured quantum Hall resistances in the topological Cd_3As_2 Dirac semimetal films. (e) Longitudinal resistance R_{xx} (red line) and transverse Hall resistance $-R_{yx}$ (black line) for a t = 12 nm thin film. Inset: primary cubic cell of Cd_3As_2. (f) As in panel (e) with R_{xx} (orange line) and $-R_{yx}$ (black line) for a t = 14 nm thin film. (g) As in panel (e) but for a t = 16 nm thicker film with R_{xx} (green line) and $-R_{yx}$ (black line). (h) As in panel (e) but for a t = 23 nm thicker film with R_{xx} (blue line) and $-R_{yx}$ (black line). In panels (e)-(h) the numbers of the horizontal bars indicate the filling factor f. Adapted from [148]. (i) The crystallographic directions ([100] along x, [010] along y and [001] along z) of the topological Cd_3As_2 Dirac semimetal together with the coordinate system used for its modeling. $(\alpha, \theta) = (-\pi/4, \arctan\sqrt{2})$ correspond to the slab growth direction [112] and $(\alpha, \theta) = (-\pi/4, 0)$ to the [110] one. y' is the growth direction of the slab and the Hall conductance is defined in the x'-z' plane. The angle ξ expresses the angle of rotation of **B** from the y' to the x' direction in the x'-y'-z' coordinate system. (l) Calculated sheet Hall conductivity of Cd_3As_2 at the Dirac node E_w according to Eq.(7) with $E_w = E_F$ as a function of $1/B$ for different orientations of the magnetic field. Adapted from [125].

 doi:10.20944/preprints202311.0757.v1

4. Conclusions

In this review article, the magnetotransport properties of topological semimetals, prototypes of high-mobility materials, have been reviewed based on the recent theoretical and experimental work done during the last two decades on this novel class of materials. The relationship between carrier mobility, electrical conductivity and MR effect shows that high-mobility topological semimetals exhibit huge MR, especially in the Hall configuration even at low external magnetic fields, and could be excellent candidates to design MR-based high-precision magnetic quantum sensors. The high mobility is also at the basis of another recently discovered effect, the 3D quantum Hall effect in some types of topological Weyl and Dirac semimetals which can be considered the 3D version of the widely known 2D quantum Hall effect. This could boost the research trends towards the full understanding of the subtle physics which governs 3D topological systems and would extend the search for device applications related to 3D systems.

More generally, the profound implications of high-mobility semimetal features on the observed MR effect and on the 3D quantum Hall effect together with the consolidated knowledge of the well-known magnetotransport properties of semiconductors and graphene could potentially open the way for novel fields of investigations in materials science.

Author Contributions: R.Z. led the conceptualization, supervised the investigation and contributed writing of the original manuscript; S.L. collected the data and contributed to the writing and editing of the manuscript; J.L. collected the data and contributed to the writing and editing of the manuscript.

Funding: R.Z. acknowledges support by the Consorzio Futuro in Ricerca (CFR) and by Gruppo Nazionale per la Fisica Matematica (GNFM-INdAM). S.L. and J.L. acknowledges support by Silicon Austria Labs (SAL), owned by the Republic of Austria, the Styrian Business Promotion Agency (SFG), the federal state of Carinthia, the Upper Austrian Research (UAR), and the Austrian Association for the Electric and Electronics Industry (FEEI).

Conflicts of Interest: The authors declare no conflict of interest.

Abbreviations

The following abbreviations are used in this manuscript:

DFT	Density functional theory
MR	Magnetoresistance

References

1. Harrison, W.A.W.A. *Electronic structure and the properties of solids : the physics of the chemical bond*; Dover Publications, 1980.
2. Ashcroft, N.W.; Mermin, N.D. *Solid State Physics*; Thomson Learning, 2021.
3. Kittel, C. 8th Edition. *Introduction to Solid State Physics*; John Wiley & Sons Inc., 2004.
4. Novoselov, K.S.; Geim, A.K.; Morozov, S.V.; Jiang, D.; Katsnelson, M.I.; Grigorieva, I.V.; Dubonos, S.V.; Firsov, A.A. Two-dimensional gas of massless Dirac fermions in graphene. *Nature* **2005**, *438*, 197–200. doi:10.1038/nature04233.
5. Geim, A.K.; Novoselov, K.S. The rise of graphene. *Nature Materials* **2007**, *6*, 183–191. doi:10.1038/nmat1849.
6. Das Sarma, S.; Hwang, E.H. Density-dependent electrical conductivity in suspended graphene: Approaching the Dirac point in transport. *Physical Review B* **2013**, *87*, 035415. doi:10.1103/PhysRevB.87.035415.
7. Du, X.; Skachko, I.; Barker, A.; Andrei, E.Y. Approaching ballistic transport in suspended graphene. *Nature Nanotechnology* **2008**, *3*, 491–495. doi:10.1038/nnano.2008.199.
8. Cho, S.; Fuhrer, M.S. Charge transport and inhomogeneity near the minimum conductivity point in graphene. *Physical Review B* **2008**, *77*, 081402. doi:10.1103/PhysRevB.77.081402.
9. Hwang, E.H.; Adam, S.; Sarma, S.D. Carrier Transport in Two-Dimensional Graphene Layers. *Physical Review Letters* **2007**, *98*, 186806. doi:10.1103/PhysRevLett.98.186806.
10. Martin, J.; Akerman, N.; Ulbricht, G.; Lohmann, T.; Smet, J.H.; von Klitzing, K.; Yacoby, A. Observation of electron–hole puddles in graphene using a scanning single-electron transistor. *Nature Physics* **2008**, *4*, 144–148. doi:10.1038/nphys781.

11. Meyer, J.C.; Geim, A.K.; Katsnelson, M.I.; Novoselov, K.S.; Booth, T.J.; Roth, S. The structure of suspended graphene sheets. *Nature* **2007**, *446*, 60–63. doi:10.1038/nature05545.
12. Bolotin, K.I.; Sikes, K.J.; Jiang, Z.; Klima, M.; Fudenberg, G.; Hone, J.; Kim, P.; Stormer, H.L. Ultrahigh electron mobility in suspended graphene. *Solid State Communications* **2008**, *146*, 351–355. doi:10.1016/j.ssc.2008.02.024.
13. Bolotin, K.I.; Sikes, K.J.; Hone, J.; Stormer, H.L.; Kim, P. Temperature-Dependent Transport in Suspended Graphene. *Physical Review Letters* **2008**, *101*, 096802. doi:10.1103/PhysRevLett.101.096802.
14. Moore, J.E. The birth of topological insulators. *Nature* **2010**, *464*, 194–198. doi:10.1038/nature08916.
15. Ando, Y. Topological Insulator Materials. *Journal of the Physical Society of Japan* **2013**, *82*, 102001. doi:10.7566/JPSJ.82.102001.
16. Hasan, M.Z.; Moore, J.E. Three-Dimensional Topological Insulators. *Annual Review of Condensed Matter Physics* **2011**, *2*, 55–78. doi:10.1146/annurev-conmatphys-062910-140432.
17. Zhu, Z.; Winkler, G.W.; Wu, Q.; Li, J.; Soluyanov, A.A. Triple Point Topological Metals. *Physical Review X* **2016**, *6*, 031003. doi:10.1103/PhysRevX.6.031003.
18. Vergniory, M.G.; Elcoro, L.; Felser, C.; Regnault, N.; Bernevig, B.A.; Wang, Z. A complete catalogue of high-quality topological materials. *Nature* **2019**, *566*, 480–485. doi:10.1038/s41586-019-0954-4.
19. Zhang, T.; Jiang, Y.; Song, Z.; Huang, H.; He, Y.; Fang, Z.; Weng, H.; Fang, C. Catalogue of topological electronic materials. *Nature* **2019**, *566*, 475–479. doi:10.1038/s41586-019-0944-6.
20. Lu, H.; Jia, S. Crystal growth and electrical transport properties of niobium and tantalum monopnictide and dipnictide semimetals. *Frontiers of Physics* **2017**, *12*, 127211. doi:10.1007/s11467-017-0692-8.
21. Niu, Q. Advances on topological materials. *Frontiers of Physics* **2020**, *15*, 43601. doi:10.1007/s11467-020-0979-z.
22. Armitage, N.; Mele, E.; Vishwanath, A. Weyl and Dirac semimetals in three-dimensional solids. *Reviews of Modern Physics* **2018**, *90*, 015001. doi:10.1103/RevModPhys.90.015001.
23. Soluyanov, A.A.; Gresch, D.; Wang, Z.; Wu, Q.; Troyer, M.; Dai, X.; Bernevig, B.A. Type-II Weyl semimetals. *Nature* **2015**, *527*, 495–498. doi:10.1038/nature15768.
24. Lv, B.; Qian, T.; Ding, H. Experimental perspective on three-dimensional topological semimetals. *Reviews of Modern Physics* **2021**, *93*, 025002. doi:10.1103/RevModPhys.93.025002.
25. Mori, R.; Wang, K.; Morimoto, T.; Ciocys, S.; Denlinger, J.D.; Paglione, J.; Lanzara, A. Observation of a Flat and Extended Surface State in a Topological Semimetal. *Materials* **2022**, *15*, 2744. doi:10.3390/ma15082744.
26. Hyart, T.; Heikkilä, T.T. Momentum-space structure of surface states in a topological semimetal with a nexus point of Dirac lines. *Physical Review B* **2016**, *93*, 235147. doi:10.1103/PhysRevB.93.235147.
27. Lv, B.; Weng, H.; Fu, B.; Wang, X.; Miao, H.; Ma, J.; Richard, P.; Huang, X.; Zhao, L.; Chen, G.; Fang, Z.; Dai, X.; Qian, T.; Ding, H. Experimental Discovery of Weyl Semimetal TaAs. *Physical Review X* **2015**, *5*, 031013. doi:10.1103/PhysRevX.5.031013.
28. Xu, S.Y.; Belopolski, I.; Alidoust, N.; Neupane, M.; Bian, G.; Zhang, C.; Sankar, R.; Chang, G.; Yuan, Z.; Lee, C.C.; Huang, S.M.; Zheng, H.; Ma, J.; Sanchez, D.S.; Wang, B.; Bansil, A.; Chou, F.; Shibayev, P.P.; Lin, H.; Jia, S.; Hasan, M.Z. Discovery of a Weyl fermion semimetal and topological Fermi arcs. *Science* **2015**, *349*, 613–617. doi:10.1126/science.aaa9297.
29. Liu, Z.K.; Yang, L.X.; Sun, Y.; Zhang, T.; Peng, H.; Yang, H.F.; Chen, C.; Zhang, Y.; Guo, Y.F.; Prabhakaran, D.; Schmidt, M.; Hussain, Z.; Mo, S.K.; Felser, C.; Yan, B.; Chen, Y.L. Evolution of the Fermi surface of Weyl semimetals in the transition metal pnictide family. *Nature Materials* **2016**, *15*, 27–31. doi:10.1038/nmat4457.
30. Li, F.Y.; Luo, X.; Dai, X.; Yu, Y.; Zhang, F.; Chen, G. Hybrid Weyl semimetal. *Physical Review B* **2016**, *94*, 121105. doi:10.1103/PhysRevB.94.121105.
31. Xu, S.Y.; Alidoust, N.; Belopolski, I.; Yuan, Z.; Bian, G.; Chang, T.R.; Zheng, H.; Strocov, V.N.; Sanchez, D.S.; Chang, G.; Zhang, C.; Mou, D.; Wu, Y.; Huang, L.; Lee, C.C.; Huang, S.M.; Wang, B.; Bansil, A.; Jeng, H.T.; Neupert, T.; Kaminski, A.; Lin, H.; Jia, S.; Zahid Hasan, M. Discovery of a Weyl fermion state with Fermi arcs in niobium arsenide. *Nature Physics* **2015**, *11*, 748–754. doi:10.1038/nphys3437.
32. Hein, P.; Jauernik, S.; Erk, H.; Yang, L.; Qi, Y.; Sun, Y.; Felser, C.; Bauer, M. Mode-resolved reciprocal space mapping of electron-phonon interaction in the Weyl semimetal candidate Td-WTe_2. *Nature Communications* **2020**, *11*, 2613. doi:10.1038/s41467-020-16076-0.
33. Yang, H.; Sun, Y.; Zhang, Y.; Shi, W.J.; Parkin, S.S.P.; Yan, B. Topological Weyl semimetals in the chiral antiferromagnetic materials Mn_3Ge and Mn_3Sn. *New Journal of Physics* **2017**, *19*, 015008. doi:10.1088/1367-2630/aa5487.

34. Lv, B.Q.; Feng, Z.L.; Xu, Q.N.; Gao, X.; Ma, J.Z.; Kong, L.Y.; Richard, P.; Huang, Y.B.; Strocov, V.N.; Fang, C.; Weng, H.M.; Shi, Y.G.; Qian, T.; Ding, H. Observation of three-component fermions in the topological semimetal molybdenum phosphide. *Nature* **2017**, *546*, 627–631. doi:10.1038/nature22390.
35. Kanagaraj, M.; Ning, J.; He, L. Topological $Co_3Sn_2S_2$ magnetic Weyl semimetal: From fundamental understanding to diverse fields of study. *Reviews in Physics* **2022**, *8*, 100072. doi:10.1016/j.revip.2022.100072.
36. Carbotte, J.P. Dirac cone tilt on interband optical background of type-I and type-II Weyl semimetals. *Physical Review B* **2016**, *94*, 165111. doi:10.1103/PhysRevB.94.165111.
37. Koepernik, K.; Kasinathan, D.; Efremov, D.V.; Khim, S.; Borisenko, S.; Büchner, B.; van den Brink, J. $TaIrTe_4$: A ternary type-II Weyl semimetal. *Physical Review B* **2016**, *93*, 201101. doi:10.1103/PhysRevB.93.201101.
38. Chang, T.R.; Xu, S.Y.; Chang, G.; Lee, C.C.; Huang, S.M.; Wang, B.; Bian, G.; Zheng, H.; Sanchez, D.S.; Belopolski, I.; Alidoust, N.; Neupane, M.; Bansil, A.; Jeng, H.T.; Lin, H.; Zahid Hasan, M. Prediction of an arc-tunable Weyl Fermion metallic state in $Mo_xW_{1-x}Te_2$. *Nature Communications* **2016**, *7*, 10639. doi:10.1038/ncomms10639.
39. Huang, S.M.; Xu, S.Y.; Belopolski, I.; Lee, C.C.; Chang, G.; Wang, B.; Alidoust, N.; Bian, G.; Neupane, M.; Zhang, C.; Jia, S.; Bansil, A.; Lin, H.; Hasan, M.Z. A Weyl Fermion semimetal with surface Fermi arcs in the transition metal monopnictide TaAs class. *Nature Communications* **2015**, *6*, 7373. doi:10.1038/ncomms8373.
40. Du, Y.; Wan, B.; Wang, D.; Sheng, L.; Duan, C.G.; Wan, X. Dirac and Weyl Semimetal in XYBi (X = Ba, Eu; Y = Cu, Ag and Au). *Scientific Reports* **2015**, *5*, 14423. doi:10.1038/srep14423.
41. Udagawa, M.; Bergholtz, E. Field-Selective Anomaly and Chiral Mode Reversal in Type-II Weyl Materials. *Physical Review Letters* **2016**, *117*, 086401. doi:10.1103/PhysRevLett.117.086401.
42. Swekis, P.; Sukhanov, A.S.; Chen, Y.C.; Gloskovskii, A.; Fecher, G.H.; Panagiotopoulos, I.; Sichelschmidt, J.; Ukleev, V.; Devishvili, A.; Vorobiev, A.; Inosov, D.S.; Goennenwein, S.T.B.; Felser, C.; Markou, A. Magnetic and Electronic Properties of Weyl Semimetal Co_2MnGa Thin Films. *Nanomaterials* **2021**, *11*, 251. doi:10.3390/nano11010251.
43. Hirschberger, M.; Kushwaha, S.; Wang, Z.; Gibson, Q.; Liang, S.; Belvin, C.A.; Bernevig, B.A.; Cava, R.J.; Ong, N.P. The chiral anomaly and thermopower of Weyl fermions in the half-Heusler GdPtBi. *Nature Materials* **2016**, *15*, 1161–1165. doi:10.1038/nmat4684.
44. Li, H.; He, H.; Lu, H.Z.; Zhang, H.; Liu, H.; Ma, R.; Fan, Z.; Shen, S.Q.; Wang, J. Negative magnetoresistance in Dirac semimetal Cd_3As_2. *Nature Communications* **2016**, *7*, 10301. doi:10.1038/ncomms10301.
45. Baidak, S.T.; Lukoyanov, A.V. Common Topological Features in Band Structure of RNiSb and RSb Compounds for R = Tb, Dy, Ho. *Materials* **2023**, *16*, 242. doi:10.3390/ma16010242.
46. Jia, S.; Xu, S.Y.; Hasan, M.Z. Weyl semimetals, Fermi arcs and chiral anomalies. *Nature Materials* **2016**, *15*, 1140–1144. doi:10.1038/nmat4787.
47. Balents, L. Weyl electrons kiss. *Physics* **2011**, *4*, 36. doi:10.1103/PhysRevB.83.205101.
48. Wan, X.; Turner, A.M.; Vishwanath, A.; Savrasov, S.Y. Topological semimetal and Fermi-arc surface states in the electronic structure of pyrochlore iridates. *Physical Review B* **2011**, *83*, 205101. doi:10.1103/PhysRevB.83.205101.
49. Deng, K.; Wan, G.; Deng, P.; Zhang, K.; Ding, S.; Wang, E.; Yan, M.; Huang, H.; Zhang, H.; Xu, Z.; Denlinger, J.; Fedorov, A.; Yang, H.; Duan, W.; Yao, H.; Wu, Y.; Fan, S.; Zhang, H.; Chen, X.; Zhou, S. Experimental observation of topological Fermi arcs in type-II Weyl semimetal $MoTe_2$. *Nature Physics* **2016**, *12*, 1105–1110. doi:10.1038/nphys3871.
50. Fang, C.; Gilbert, M.J.; Dai, X.; Bernevig, B.A. Multi-Weyl Topological Semimetals Stabilized by Point Group Symmetry. *Physical Review Letters* **2012**, *108*, 266802. doi:10.1103/PhysRevLett.108.266802.
51. Wang, Z.; Weng, H.; Wu, Q.; Dai, X.; Fang, Z. Three-dimensional Dirac semimetal and quantum transport in Cd_3As_2. *Physical Review B* **2013**, *88*, 125427. doi:10.1103/PhysRevB.88.125427.
52. Liu, Z.K.; Jiang, J.; Zhou, B.; Wang, Z.J.; Zhang, Y.; Weng, H.M.; Prabhakaran, D.; Mo, S.K.; Peng, H.; Dudin, P.; Kim, T.; Hoesch, M.; Fang, Z.; Dai, X.; Shen, Z.X.; Feng, D.L.; Hussain, Z.; Chen, Y.L. A stable three-dimensional topological Dirac semimetal Cd_3As_2. *Nature Materials* **2014**, *13*, 677–681. doi:10.1038/nmat3990.
53. Liu, Z.K.; Zhou, B.; Zhang, Y.; Wang, Z.J.; Weng, H.M.; Prabhakaran, D.; Mo, S.K.; Shen, Z.X.; Fang, Z.; Dai, X.; Hussain, Z.; Chen, Y.L. Discovery of a Three-Dimensional Topological Dirac Semimetal, Na_3Bi. *Science* **2014**, *343*, 864–867. doi:10.1126/science.1245085.

54. Mullen, K.; Uchoa, B.; Glatzhofer, D.T. Line of Dirac Nodes in Hyperhoneycomb Lattices. *Physical Review Letters* **2015**, *115*, 026403. doi:10.1103/PhysRevLett.115.026403.
55. Xie, L.S.; Schoop, L.M.; Seibel, E.M.; Gibson, Q.D.; Xie, W.; Cava, R.J. A new form of Ca_3P_2 with a ring of Dirac nodes. *APL Materials* **2015**, *3*, 083602. doi:10.1063/1.4926545.
56. Zhang, K.; Yan, M.; Zhang, H.; Huang, H.; Arita, M.; Sun, Z.; Duan, W.; Wu, Y.; Zhou, S. Experimental evidence for type-II Dirac semimetal in $PtSe_2$. *Physical Review B* **2017**, *96*, 125102. doi:10.1103/PhysRevB.96.125102.
57. Vafek, O.; Vishwanath, A. Dirac Fermions in Solids: From High-Tc Cuprates and Graphene to Topological Insulators and Weyl Semimetals. *Annual Review of Condensed Matter Physics* **2014**, *5*, 83–112. doi:10.1146/annurev-conmatphys-031113-133841.
58. Yan, M.; Huang, H.; Zhang, K.; Wang, E.; Yao, W.; Deng, K.; Wan, G.; Zhang, H.; Arita, M.; Yang, H.; Sun, Z.; Yao, H.; Wu, Y.; Fan, S.; Duan, W.; Zhou, S. Lorentz-violating type-II Dirac fermions in transition metal dichalcogenide $PtTe_2$. *Nature Communications* **2017**, *8*, 257. doi:10.1038/s41467-017-00280-6.
59. Wang, Z.; Sun, Y.; Chen, X.Q.; Franchini, C.; Xu, G.; Weng, H.; Dai, X.; Fang, Z. Dirac semimetal and topological phase transitions in A_3Bi (A=Na, K, Rb). *Physical Review B* **2012**, *85*, 195320. doi:10.1103/PhysRevB.85.195320.
60. Young, S.M.; Zaheer, S.; Teo, J.C.Y.; Kane, C.L.; Mele, E.J.; Rappe, A.M. Dirac Semimetal in Three Dimensions. *Physical Review Letters* **2012**, *108*, 140405. doi:10.1103/PhysRevLett.108.140405.
61. Gibson, Q.D.; Schoop, L.M.; Muechler, L.; Xie, L.S.; Hirschberger, M.; Ong, N.P.; Car, R.; Cava, R.J. Three-dimensional Dirac semimetals: Design principles and predictions of new materials. *Physical Review B* **2015**, *91*, 205128. doi:10.1103/PhysRevB.91.205128.
62. Xu, Q.; Yu, R.; Fang, Z.; Dai, X.; Weng, H. Topological nodal line semimetals in the CaP_3 family of materials. *Physical Review B* **2017**, *95*, 045136. doi:10.1103/PhysRevB.95.045136.
63. Yang, M.X.; Luo, W.; Chen, W. Quantum transport in topological nodal-line semimetals. *Advances in Physics: X* **2022**, *7*, 2065216. doi:10.1080/23746149.2022.2065216.
64. Chang, T.R.; Pletikosic, I.; Kong, T.; Bian, G.; Huang, A.; Denlinger, J.; Kushwaha, S.K.; Sinkovic, B.; Jeng, H.T.; Valla, T.; Xie, W.; Cava, R.J. Realization of a Type-II Nodal-Line Semimetal in Mg_3Bi_2. *Advanced Science* **2019**, *6*, 1800897. doi:10.1002/advs.201800897.
65. Du, Y.; Tang, F.; Wang, D.; Sheng, L.; Kan, E.j.; Duan, C.G.; Savrasov, S.Y.; Wan, X. CaTe: a new topological node-line and Dirac semimetal. *npj Quantum Materials* **2017**, *2*, 1–4. doi:10.1038/s41535-016-0005-4.
66. Sun, Y.; Li, J.; Zhao, H.; Wu, M.; Pan, H. Magneto-Optical Transport Properties of Type-II Nodal Line Semimetals. *Materials* **2021**, *14*, 3035. doi:10.3390/ma14113035.
67. Okamoto, Y.; Saigusa, K.; Wada, T.; Yamakawa, Y.; Yamakage, A.; Sasagawa, T.; Katayama, N.; Takatsu, H.; Kageyama, H.; Takenaka, K. High-mobility carriers induced by chemical doping in the candidate nodal-line semimetal CaAgP. *Physical Review B* **2020**, *102*, 115101. doi:10.1103/PhysRevB.102.115101.
68. Zhang, X.; Jin, L.; Dai, X.; Liu, G. Topological Type-II Nodal Line Semimetal and Dirac Semimetal State in Stable Kagome Compound Mg_3Bi_2. *The Journal of Physical Chemistry Letters* **2017**, *8*, 4814–4819. doi:10.1021/acs.jpclett.7b02129.
69. Chang, G.; Xu, S.Y.; Sanchez, D.S.; Huang, S.M.; Lee, C.C.; Chang, T.R.; Bian, G.; Zheng, H.; Belopolski, I.; Alidoust, N.; Jeng, H.T.; Bansil, A.; Lin, H.; Hasan, M.Z. A strongly robust type II Weyl fermion semimetal state in Ta_3S_2. *Science Advances* **2016**, *2*, e1600295. doi:10.1126/sciadv.1600295.
70. Song, Z.; Zhang, T.; Fang, Z.; Fang, C. Quantitative mappings between symmetry and topology in solids. *Nature Communications* **2018**, *9*, 3530. doi:10.1038/s41467-018-06010-w.
71. Song, Z.; Zhang, T.; Fang, C. Diagnosis for Nonmagnetic Topological Semimetals in the Absence of Spin-Orbital Coupling. *Physical Review X* **2018**, *8*, 031069. doi:10.1103/PhysRevX.8.031069.
72. Yu, P.Y.; Cardona, M. *Fundamentals of Semiconductors: Physics and Materials Properties*; Graduate Texts in Physics, Springer: Berlin, Heidelberg, 2010. doi:10.1007/978-3-642-00710-1.
73. Goringe, C.M.; Bowler, D.R.; Hernández, E. Tight-binding modelling of materials. *Reports on Progress in Physics* **1997**, *60*, 1447. doi:10.1088/0034-4885/60/12/001.
74. Slater, J.C.; Koster, G.F. Simplified LCAO Method for the Periodic Potential Problem. *Physical Review* **1954**, *94*, 1498–1524. doi:10.1103/PhysRev.94.1498.
75. Slater, J.C. Wave Functions in a Periodic Potential. *Physical Review* **1937**, *51*, 846–851. doi:10.1103/PhysRev.51.846.

76. Kresse, G.; Furthmüller, J. Efficiency of ab-initio total energy calculations for metals and semiconductors using a plane-wave basis set. *Computational Materials Science* **1996**, *6*, 15–50. doi:10.1016/0927-0256(96)00008-0.
77. Kresse, G.; Furthmüller, J. Efficient iterative schemes for ab initio total-energy calculations using a plane-wave basis set. *Physical Review B* **1996**, *54*, 11169–11186. doi:10.1103/PhysRevB.54.11169.
78. Hohenberg, P.; Kohn, W. Inhomogeneous Electron Gas. *Physical Review* **1964**, *136*, B864–B871. doi:10.1103/PhysRev.136.B864.
79. Kohn, W.; Sham, L.J. Self-Consistent Equations Including Exchange and Correlation Effects. *Physical Review* **1965**, *140*, A1133–A1138. doi:10.1103/PhysRev.140.A1133.
80. Parr, R.G.; Weitao, Y. Title Pages. In *Density-Functional Theory of Atoms and Molecules*; Parr, R.G.; Weitao, Y., Eds.; Oxford University Press, 1995; p. 0. doi:10.1093/oso/9780195092769.002.0001.
81. Dreizler, R.M.; Gross, E.K.U. *Density Functional Theory*; Springer: Berlin, Heidelberg, 1990. doi:10.1007/978-3-642-86105-5.
82. Blöchl, P.E. Projector augmented-wave method. *Physical Review B* **1994**, *50*, 17953–17979. doi:10.1103/PhysRevB.50.17953.
83. Andersen, O.K. Linear methods in band theory. *Physical Review B* **1975**, *12*, 3060–3083. doi:10.1103/PhysRevB.12.3060.
84. Singh, D.J.; Nordström, L. *Planewaves, Pseudopotentials and the LAPW Method*; Springer US, 2006. doi:10.1007/978-0-387-29684-5.
85. Wimmer, E.; Krakauer, H.; Weinert, M.; Freeman, A.J. Full-potential self-consistent linearized-augmented-plane-wave method for calculating the electronic structure of molecules and surfaces: O_2 molecule. *Physical Review B* **1981**, *24*, 864–875. doi:10.1103/PhysRevB.24.864.
86. Burkov, A.A. Topological semimetals. *Nature Materials* **2016**, *15*, 1145–1148. doi:10.1038/nmat4788.
87. Tang, F.; Wan, X. Effective models for nearly ideal Dirac semimetals. *Frontiers of Physics* **2019**, *14*, 43603. doi:10.1007/s11467-019-0902-7.
88. He, L.; Hong, X.; Dong, J.; Pan, J.; Zhang, Z.; Zhang, J.; Li, S. Quantum Transport Evidence for the Three-Dimensional Dirac Semimetal Phase in Cd_3As_2. *Physical Review Letters* **2014**, *113*, 246402. doi:10.1103/PhysRevLett.113.246402.
89. Fei, F.; Bo, X.; Wang, R.; Wu, B.; Jiang, J.; Fu, D.; Gao, M.; Zheng, H.; Chen, Y.; Wang, X.; Bu, H.; Song, F.; Wan, X.; Wang, B.; Wang, G. Nontrivial Berry phase and type-II Dirac transport in the layered material $PdTe_2$. *Physical Review B* **2017**, *96*, 041201. doi:10.1103/PhysRevB.96.041201.
90. Guo, P.J.; Yang, H.C.; Liu, K.; Lu, Z.Y. Type-II Dirac semimetals in the YPd_2Sn. *Physical Review B* **2017**, *95*, 155112. doi:10.1103/PhysRevB.95.155112.
91. Shekhar, C.; Nayak, A.K.; Sun, Y.; Schmidt, M.; Nicklas, M.; Leermakers, I.; Zeitler, U.; Skourski, Y.; Wosnitza, J.; Liu, Z.; Chen, Y.; Schnelle, W.; Borrmann, H.; Grin, Y.; Felser, C.; Yan, B. Extremely large magnetoresistance and ultrahigh mobility in the topological Weyl semimetal candidate NbP. *Nature Physics* **2015**, *11*, 645–649. doi:10.1038/nphys3372.
92. Weng, H.; Fang, C.; Fang, Z.; Bernevig, B.A.; Dai, X. Weyl Semimetal Phase in Noncentrosymmetric Transition-Metal Monophosphides. *Physical Review X* **2015**, *5*, 011029. doi:10.1103/PhysRevX.5.011029.
93. Zhu, Z.; Yan, D.; Nie, X.A.; Xu, H.K.; Yang, X.; Guan, D.D.; Wang, S.; Li, Y.Y.; Liu, C.; Liu, J.W.; Luo, H.X.; Zheng, H.; Jia, J.F. Scanning tunneling microscopic investigation on morphology of magnetic Weyl semimetal $YbMnBi_2$ *. *Chinese Physics B* **2019**, *28*, 077302. doi:10.1088/1674-1056/28/7/077302.
94. Sie, E.J.; Nyby, C.M.; Pemmaraju, C.D.; Park, S.J.; Shen, X.; Yang, J.; Hoffmann, M.C.; Ofori-Okai, B.K.; Li, R.; Reid, A.H.; Weathersby, S.; Mannebach, E.; Finney, N.; Rhodes, D.; Chenet, D.; Antony, A.; Balicas, L.; Hone, J.; Devereaux, T.P.; Heinz, T.F.; Wang, X.; Lindenberg, A.M. An ultrafast symmetry switch in a Weyl semimetal. *Nature* **2019**, *565*, 61–66. doi:10.1038/s41586-018-0809-4.
95. Burkov, A.A.; Balents, L. Weyl Semimetal in a Topological Insulator Multilayer. *Physical Review Letters* **2011**, *107*, 127205. doi:10.1103/PhysRevLett.107.127205.
96. Zhang, C.L.; Yuan, Z.; Jiang, Q.D.; Tong, B.; Zhang, C.; Xie, X.C.; Jia, S. Electron scattering in tantalum monoarsenide. *Physical Review B* **2017**, *95*, 085202. doi:10.1103/PhysRevB.95.085202.
97. Kumar, N.; Sun, Y.; Nicklas, M.; Watzman, S.J.; Young, O.; Leermakers, I.; Hornung, J.; Klotz, J.; Gooth, J.; Manna, K.; Süß, V.; Guin, S.N.; Förster, T.; Schmidt, M.; Muechler, L.; Yan, B.; Werner, P.; Schnelle, W.; Zeitler,

U.; Wosnitza, J.; Parkin, S.S.P.; Felser, C.; Shekhar, C. Extremely high conductivity observed in the triple point topological metal MoP. *Nature Communications* **2019**, *10*, 2475. doi:10.1038/s41467-019-10126-y.

98. Chen, Z.G.; Zhang, C.; Zou, Y.; Zhang, E.; Yang, L.; Hong, M.; Xiu, F.; Zou, J. Scalable Growth of High Mobility Dirac Semimetal Cd_3As_2 Microbelts. *Nano Letters* **2015**, *15*, 5830–5834. doi:10.1021/acs.nanolett.5b01885.
99. Sugihara, K.; Kawamuma, K.; Tsuzuku, T. Temperature Dependence of the Average Mobility in Graphite. *Journal of the Physical Society of Japan* **1979**, *47*, 1210–1215. doi:10.1143/JPSJ.47.1210.
100. Pendrys, L.A.; Zeller, C.; Vogel, F.L. Electrical transport properties of natural and synthetic graphite. *Journal of Materials Science* **1980**, *15*, 2103–2112. doi:10.1007/BF00550638.
101. Ibach, H.; Lüth, H. *Solid-State Physics: An Introduction to Principles of Materials Science ; with 100 Problems*; Springer, 1995.
102. Neupane, M.; Xu, S.Y.; Sankar, R.; Alidoust, N.; Bian, G.; Liu, C.; Belopolski, I.; Chang, T.R.; Jeng, H.T.; Lin, H.; Bansil, A.; Chou, F.; Hasan, M.Z. Observation of a three-dimensional topological Dirac semimetal phase in high-mobility Cd_3As_2. *Nature Communications* **2014**, *5*, 3786. doi:10.1038/ncomms4786.
103. Hosur, P.; Qi, X. Recent developments in transport phenomena in Weyl semimetals. *Comptes Rendus Physique* **2013**, *14*, 857–870. doi:10.1016/j.crhy.2013.10.010.
104. Khim, S.; Koepernik, K.; Efremov, D.V.; Klotz, J.; Förster, T.; Wosnitza, J.; Sturza, M.I.; Wurmehl, S.; Hess, C.; van den Brink, J.; Büchner, B. Magnetotransport and de Haas–van Alphen measurements in the type-II Weyl semimetal $TaIrTe_4$. *Physical Review B* **2016**, *94*, 165145. doi:10.1103/PhysRevB.94.165145.
105. Bradlyn, B.; Cano, J.; Wang, Z.; Vergniory, M.G.; Felser, C.; Cava, R.J.; Bernevig, B.A. Beyond Dirac and Weyl fermions: Unconventional quasiparticles in conventional crystals. *Science* **2016**, *353*, aaf5037. doi:10.1126/science.aaf5037.
106. Huang, S.M.; Xu, S.Y.; Belopolski, I.; Lee, C.C.; Chang, G.; Wang, B.; Alidoust, N.; Bian, G.; Neupane, M.; Zhang, C.; Jia, S.; Bansil, A.; Lin, H.; Hasan, M.Z. A Weyl Fermion semimetal with surface Fermi arcs in the transition metal monopnictide TaAs class. *Nature Communications* **2015**, *6*, 7373. doi:10.1038/ncomms8373.
107. Li, S.; Yu, Z.M.; Yao, Y.; Yang, S.A. Type-II topological metals. *Frontiers of Physics* **2020**, *15*, 43201. doi:10.1007/s11467-020-0963-7.
108. Li, P.; Wen, Y.; He, X.; Zhang, Q.; Xia, C.; Yu, Z.M.; Yang, S.A.; Zhu, Z.; Alshareef, H.N.; Zhang, X.X. Evidence for topological type-II Weyl semimetal WTe_2. *Nature Communications* **2017**, *8*, 2150. doi:10.1038/s41467-017-02237-1.
109. Autès, G.; Gresch, D.; Troyer, M.; Soluyanov, A.; Yazyev, O. Robust Type-II Weyl Semimetal Phase in Transition Metal Diphosphides XP_2 (X=Mo, W). *Physical Review Letters* **2016**, *117*, 066402. doi:10.1103/PhysRevLett.117.066402.
110. Tamai, A.; Wu, Q.; Cucchi, I.; Bruno, F.; Riccò, S.; Kim, T.; Hoesch, M.; Barreteau, C.; Giannini, E.; Besnard, C.; Soluyanov, A.; Baumberger, F. Fermi Arcs and Their Topological Character in the Candidate Type-II Weyl Semimetal $MoTe_2$. *Physical Review X* **2016**, *6*, 031021. doi:10.1103/PhysRevX.6.031021.
111. Belopolski, I.; Sanchez, D.S.; Ishida, Y.; Pan, X.; Yu, P.; Xu, S.Y.; Chang, G.; Chang, T.R.; Zheng, H.; Alidoust, N.; Bian, G.; Neupane, M.; Huang, S.M.; Lee, C.C.; Song, Y.; Bu, H.; Wang, G.; Li, S.; Eda, G.; Jeng, H.T.; Kondo, T.; Lin, H.; Liu, Z.; Song, F.; Shin, S.; Hasan, M.Z. Discovery of a new type of topological Weyl fermion semimetal state in $Mo_xW_{1-x}Te_2$. *Nature Communications* **2016**, *7*, 13643. doi:10.1038/ncomms13643.
112. Zyuzin, A.A.; Tiwari, R.P. Intrinsic anomalous Hall effect in type-II Weyl semimetals. *JETP Letters* **2016**, *103*, 717–722. doi:10.1134/S002136401611014X.
113. Haubold, E.; Koepernik, K.; Efremov, D.; Khim, S.; Fedorov, A.; Kushnirenko, Y.; van den Brink, J.; Wurmehl, S.; Büchner, B.; Kim, T.K.; Hoesch, M.; Sumida, K.; Taguchi, K.; Yoshikawa, T.; Kimura, A.; Okuda, T.; Borisenko, S.V. Experimental realization of type-II Weyl state in noncentrosymmetric $TaIrTe_4$. *Physical Review B* **2017**, *95*, 241108. doi:10.1103/PhysRevB.95.241108.
114. Islam, M.R.; Mojumder, M.R.H.; Moghal, B.K.; Islam, A.S.M.J.; Miah, M.R.; Roy, S.; Kumar, A.; Shihavuddin, A.S.M.; Ashique, R.H. Impact of strain on the electronic, phonon, and optical properties of monolayer transition metal dichalcogenides XTe_2 (X = Mo and W). *Physica Scripta* **2022**, *97*, 045806. doi:10.1088/1402-4896/ac57e0.
115. Borisenko, S.; Evtushinsky, D.; Gibson, Q.; Yaresko, A.; Koepernik, K.; Kim, T.; Ali, M.; van den Brink, J.; Hoesch, M.; Fedorov, A.; Haubold, E.; Kushnirenko, Y.; Soldatov, I.; Schäfer, R.; Cava, R.J. Time-reversal symmetry breaking type-II Weyl state in $YbMnBi_2$. *Nature Communications* **2019**, *10*, 3424. doi:10.1038/s41467-019-11393-5.

116. Tchoumakov, S.; Civelli, M.; Goerbig, M.O. Magnetic-Field-Induced Relativistic Properties in Type-I and Type-II Weyl Semimetals. *Physical Review Letters* **2016**, *117*, 086402. doi:10.1103/PhysRevLett.117.086402.
117. Bedoya-Pinto, A.; Pandeya, A.K.; Liu, D.; Deniz, H.; Chang, K.; Tan, H.; Han, H.; Jena, J.; Kostanovskiy, I.; Parkin, S.S.P. Realization of Epitaxial NbP and TaP Weyl Semimetal Thin Films. *ACS Nano* **2020**, *14*, 4405–4413. doi:10.1021/acsnano.9b09997.
118. Lv, H.Y.; Lu, W.J.; Shao, D.F.; Liu, Y.; Tan, S.G.; Sun, Y.P. Perfect charge compensation in WTe_2 for the extraordinary magnetoresistance: From bulk to monolayer. *Europhysics Letters* **2015**, *110*, 37004. doi:10.1209/0295-5075/110/37004.
119. Tian, W.; Yu, W.; Liu, X.; Wang, Y.; Shi, J. A Review of the Characteristics, Synthesis, and Thermodynamics of Type-II Weyl Semimetal WTe_2. *Materials* **2018**, *11*, 1185. doi:10.3390/ma11071185.
120. Rosmus, M.; Olszowska, N.; Bukowski, Z.; Starowicz, P.; Piekarz, P.; Ptok, A. Electronic Band Structure and Surface States in Dirac Semimetal $LaAgSb_2$. *Materials* **2022**, *15*, 7168. doi:10.3390/ma15207168.
121. Wadge, A.S.; Grabecki, G.; Autieri, C.; Kowalski, B.J.; Iwanowski, P.; Cuono, G.; Islam, M.F.; Canali, C.M.; Dybko, K.; Hruban, A.; Łusakowski, A.; Wojciechowski, T.; Diduszko, R.; Lynnyk, A.; Olszowska, N.; Rosmus, M.; Kołodziej, J.; Wiśniewski, A. Electronic properties of $TaAs_2$ topological semimetal investigated by transport and ARPES. *Journal of Physics: Condensed Matter* **2022**, *34*, 125601. doi:10.1088/1361-648X/ac43fe.
122. Mathur, P.C.; Kataria, N.D.; Jain, S.; Sharma, V. Electron mobility in n-InSb from 77 to 300K. *Journal of Physics C: Solid State Physics* **1975**, *9*, L89. doi:10.1088/0022-3719/9/4/002.
123. Pei, Q.L.; Luo, X.; Chen, F.C.; Lv, H.Y.; Sun, Y.; Lu, W.J.; Tong, P.; Sheng, Z.G.; Han, Y.Y.; Song, W.H.; Zhu, X.B.; Sun, Y.P. Mobility spectrum analytical approach for the type-II Weyl semimetal Td-$MoTe_2$. *Applied Physics Letters* **2018**, *112*, 072401. doi:10.1063/1.5008850.
124. Ishiwata, S.; Shiomi, Y.; Lee, J.S.; Bahramy, M.S.; Suzuki, T.; Uchida, M.; Arita, R.; Taguchi, Y.; Tokura, Y. Extremely high electron mobility in a phonon-glass semimetal. *Nature Materials* **2013**, *12*, 512–517. doi:10.1038/nmat3621.
125. Wang, C.M.; Sun, H.P.; Lu, H.Z.; Xie, X.C. 3D Quantum Hall Effect of Fermi Arcs in Topological Semimetals. *Phys. Rev. Lett.* **2017**, *119*, 136806. doi:10.1103/PhysRevLett.119.136806.
126. Kumar, N.; Sun, Y.; Xu, N.; Manna, K.; Yao, M.; Süss, V.; Leermakers, I.; Young, O.; Förster, T.; Schmidt, M.; Borrmann, H.; Yan, B.; Zeitler, U.; Shi, M.; Felser, C.; Shekhar, C. Extremely high magnetoresistance and conductivity in the type-II Weyl semimetals WP_2 and MoP_2. *Nature Communications* **2017**, *8*, 1642. doi:10.1038/s41467-017-01758-z.
127. Liang, T.; Gibson, Q.; Ali, M.N.; Liu, M.; Cava, R.J.; Ong, N.P. Ultrahigh mobility and giant magnetoresistance in the Dirac semimetal Cd_3As_2. *Nature Materials* **2015**, *14*, 280–284. doi:10.1038/nmat4143.
128. Feng, J.; Pang, Y.; Wu, D.; Wang, Z.; Weng, H.; Li, J.; Dai, X.; Fang, Z.; Shi, Y.; Lu, L. Large linear magnetoresistance in Dirac semimetal Cd_3As_2 with Fermi surfaces close to the Dirac points. *Physical Review B* **2015**, *92*, 081306. doi:10.1103/PhysRevB.92.081306.
129. Pletikosić, I.; Ali, M.N.; Fedorov, A.V.; Cava, R.J.; Valla, T. Electronic structure basis for the extraordinary magnetoresistance in WTe_2. *Physical review letters* **2014**, *113*, 216601. doi:10.1103/PhysRevLett.113.216601.
130. Ali, M.N.; Xiong, J.; Flynn, S.; Tao, J.; Gibson, Q.D.; Schoop, L.M.; Liang, T.; Haldolaarachchige, N.; Hirschberger, M.; Ong, N.P.; Cava, R.J. Large, non-saturating magnetoresistance in WTe_2. *Nature* **2014**, *514*, 205–208. doi:10.1038/nature13763.
131. Yu, Z.M.; Yao, Y.; Yang, S.A. Predicted Unusual Magnetoresponse in Type-II Weyl Semimetals. *Physical Review Letters* **2016**, *117*, 077202. doi:10.1103/PhysRevLett.117.077202.
132. Adhikari, R.; Adhikari, S.; Faina, B.; Terschanski, M.; Bork, S.; Leimhofer, C.; Cinchetti, M.; Bonanni, A. Positive Magnetoresistance and Chiral Anomaly in Exfoliated Type-II Weyl Semimetal Td-WTe_2. *Nanomaterials* **2021**, *11*, 2755. doi:10.3390/nano11102755.
133. Singha, R.; Pariari, A.K.; Satpati, B.; Mandal, P. Large nonsaturating magnetoresistance and signature of nondegenerate Dirac nodes in ZrSiS. *Proceedings of the National Academy of Sciences* **2017**, *114*, 2468–2473. doi:10.1073/pnas.1618004114.
134. Shekhar, C.; Ouardi, S.; Nayak, A.K.; Fecher, G.H.; Schnelle, W.; Felser, C. Ultrahigh mobility and nonsaturating magnetoresistance in Heusler topological insulators. *Physical Review B* **2012**, *86*, 155314. doi:10.1103/PhysRevB.86.155314.
135. Singleton, J.; Singleton, J. *Band Theory and Electronic Properties of Solids*; Oxford Master Series in Physics, Oxford University Press: Oxford, New York, 2001.

136. Yang, J.; Song, Z.Y.; Guo, L.; Gao, H.; Dong, Z.; Yu, Q.; Zheng, R.K.; Kang, T.T.; Zhang, K. Nontrivial Giant Linear Magnetoresistance in Nodal-Line Semimetal ZrGeSe 2D Layers. *Nano Letters* **2021**, *21*, 10139–10145. doi:10.1021/acs.nanolett.1c01647.
137. Arnold, F.; Shekhar, C.; Wu, S.C.; Sun, Y.; dos Reis, R.D.; Kumar, N.; Naumann, M.; Ajeesh, M.O.; Schmidt, M.; Grushin, A.G.; Bardarson, J.H.; Baenitz, M.; Sokolov, D.; Borrmann, H.; Nicklas, M.; Felser, C.; Hassinger, E.; Yan, B. Negative magnetoresistance without well-defined chirality in the Weyl semimetal TaP. *Nature Communications* **2016**, *7*, 11615. doi:10.1038/ncomms11615.
138. Son, D.T.; Spivak, B.Z. Chiral anomaly and classical negative magnetoresistance of Weyl metals. *Physical Review B* **2013**, *88*, 104412. doi:10.1103/PhysRevB.88.104412.
139. Wang, K.; Graf, D.; Li, L.; Wang, L.; Petrovic, C. Anisotropic giant magnetoresistance in $NbSb_2$. *Scientific Reports* **2014**, *4*, 7328. doi:10.1038/srep07328.
140. Li, P.; Qiu, P.; Xu, Q.; Luo, J.; Xiong, Y.; Xiao, J.; Aryal, N.; Li, Q.; Chen, L.; Shi, X. Colossal Nernst power factor in topological semimetal $NbSb_2$. *Nature Communications* **2022**, *13*, 7612. doi:10.1038/s41467-022-35289-z.
141. Ghimire, N.J.; Luo, Y.; Neupane, M.; Williams, D.J.; Bauer, E.D.; Ronning, F. Magnetotransport of single crystalline NbAs. *Journal of Physics: Condensed Matter* **2015**, *27*, 152201. doi:10.1088/0953-8984/27/15/152201.
142. Kumar, P.; Sudesh.; Patnaik, S. Exceptional magnetoresistance in Weyl semimetal TaP. *AIP Conference Proceedings* **2019**, *2115*, 030409. doi:10.1063/1.5113248.
143. Shekhar, C.; Süss, V.; Schmidt, M. Mobility induced unsaturated high linear magnetoresistance in transition-metal monopnictides Weyl semimetals, 2016, [arXiv:cond-mat.mtrl-sci/1606.06649].
144. Wang, Y.; Wang, L.; Liu, X.; Wu, H.; Wang, P.; Yan, D.; Cheng, B.; Shi, Y.; Watanabe, K.; Taniguchi, T.; Liang, S.J.; Miao, F. Direct Evidence for Charge Compensation-Induced Large Magnetoresistance in Thin WTe_2. *Nano Letters* **2019**, *19*, 3969–3975. doi:10.1021/acs.nanolett.9b01275.
145. Mun, E.; Ko, H.; Miller, G.J.; Samolyuk, G.D.; Bud'ko, S.L.; Canfield, P.C. Magnetic field effects on transport properties of $PtSn_4$. *Physical Review B* **2012**, *85*, 035135. doi:10.1103/PhysRevB.85.035135.
146. Fu, C.; Guin, S.N.; Scaffidi, T.; Sun, Y.; Saha, R.; Watzman, S.J.; Srivastava, A.K.; Li, G.; Schnelle, W.; Parkin, S.S.P.; Felser, C.; Gooth, J. Largely Suppressed Magneto-Thermal Conductivity and Enhanced Magneto-Thermoelectric Properties in $PtSn_4$. *Research* **2020**, *2020*. doi:10.34133/2020/4643507.
147. Gao, W.; Hao, N.; Zheng, F.W.; Ning, W.; Wu, M.; Zhu, X.; Zheng, G.; Zhang, J.; Lu, J.; Zhang, H.; Xi, C.; Yang, J.; Du, H.; Zhang, P.; Zhang, Y.; Tian, M. Extremely Large Magnetoresistance in a Topological Semimetal Candidate Pyrite $PtBi_2$. *Physical Review Letters* **2017**, *118*, 256601. doi:10.1103/PhysRevLett.118.256601.
148. Uchida, M.; Nakazawa, Y.; Nishihaya, S.; Akiba, K.; Kriener, M.; Kozuka, Y.; Miyake, A.; Taguchi, Y.; Tokunaga, M.; Nagaosa, N.; Tokura, Y.; Kawasaki, M. Quantum Hall states observed in thin films of Dirac semimetal Cd3As2. *Nature Communications* **2017**, *8*, 2274. doi:10.1038/s41467-017-02423-1.
149. Zhang, C.; Zhang, Y.; Yuan, X.; Lu, S.; Zhang, J.; Narayan, A.; Liu, Y.; Zhang, H.; Ni, Z.; Liu, R.; Choi, E.S.; Suslov, A.; Sanvito, S.; Pi, L.; Lu, H.Z.; Potter, A.C.; Xiu, F. Quantum Hall effect based on Weyl orbits in Cd3As2. *Nature* **2019**, *565*, 331–336. doi:10.1038/s41586-018-0798-3.
150. Weis, J. Quantum Hall Effect. In *Encyclopedia of Condensed Matter Physics*; Bassani, F.; Liedl, G.L.; Wyder, P., Eds.; Elsevier: Oxford, 2005; pp. 22–29. doi:https://doi.org/10.1016/B0-12-369401-9/00730-0.
151. Klitzing, K.v.; Dorda, G.; Pepper, M. New Method for High-Accuracy Determination of the Fine-Structure Constant Based on Quantized Hall Resistance. *Phys. Rev. Lett.* **1980**, *45*, 494–497. doi:10.1103/PhysRevLett.45.494.
152. Laughlin, R.B. Quantized Hall conductivity in two dimensions. *Phys. Rev. B* **1981**, *23*, 5632–5633. doi:10.1103/PhysRevB.23.5632.